The Astrophysical Journal, 866:77 (21pp), 2018 October 20 https://doi.org/10.3847/1538-4357/aae07e
© 2018. The American Astronomical Society. All rights reserved.

Molecular Gas and Star Formation Properties in Early Stage Mergers: SMA CO(2-1) Observations of the LIRGs NGC 3110 and NGC 232

Daniel Espada[1,2], Sergio Martin[3,4], Simon Verley[5,6], Alex R. Pettitt[7], Satoki Matsushita[8], Maria Argudo-Fernández[9,10], Zara Randriamanakoto[11], Pei-Ying Hsieh[12], Toshiki Saito[1,13], Rie E. Miura[1], Yuka Kawana[14,15], Jose Sabater[16], Lourdes Verdes-Montenegro[17], Paul T. P. Ho[12,18], Ryohei Kawabe[1,2], and Daisuke Iono[1,2]

[1] National Astronomical Observatory of Japan, 2-21-1 Osawa, Mitaka, Tokyo 181-8588, Japan; daniel.espada@nao.ac.jp
[2] The Graduate University for Advanced Studies (SOKENDAI), 2-21-1 Osawa, Mitaka, Tokyo, 181-0015, Japan
[3] Joint ALMA Observatory, Alonso de Córdova, 3107, Vitacura, Santiago 763-0355, Chile
[4] European Southern Observatory, Alonso de Córdova 3107, Vitacura, Santiago 763-0355, Chile
[5] Departamento de Física Teórica y del Cosmos, Universidad de Granada, E-18010 Granada, Spain
[6] Instituto Universitario Carlos I de Física Teórica y Computacional, Facultad de Ciencias, E-18071 Granada, Spain
[7] Department of Physics, Faculty of Science, Hokkaido University, Kita 10 Nishi 8 Kita-ku, Sapporo 060-0810, Japan
[8] Academia Sinica Institute of Astronomy and Astrophysics, 11F of Astro-Math Bldg, AS/NTU, No.1, Section 4, Roosevelt Rd, Taipei 10617, Taiwan, Republic of China
[9] Centro de Astronomía, Universidad de Antofagasta, Avenida Angamos 601, Antofagasta 1270300, Chile
[10] Chinese Academy of Sciences South America Center for Astronomy, China-Chile Joint Center for Astronomy, Camino El Observatorio, 1515, Las Condes, Santiago, Chile
[11] Department of Astronomy, University of Cape Town, Private Bag X3, Rondebosch 7701, South Africa
[12] Academia Sinica Institute of Astronomy and Astrophysics, P.O. Box 23-141, Taipei 10617, Taiwan, Republic of China
[13] Max-Planck-Institut für Astronomie, Königstuhl 17, D-69117 Heidelberg, Germany
[14] Japan Women's University, 2-8-1 Mejirodai, Bunkyo, Tokyo, 112-8681, Japan
[15] Tokyo Metropolitan Mihara High School, 1-33-1, Omorihigashi, Ota-ku, Tokyo, Japan
[16] Institute for Astronomy, University of Edinburgh, EH9 3, HJ Edinburgh, UK
[17] Instituto de Astrofísica de Andalucía (CSIC), Apdo. 3004, E-18008, Granada, Spain
[18] East Asian Observatory, 660 North Aohoku Place, University Park, Hilo, HI 96720, USA

Received 2018 May 23; revised 2018 September 4; accepted 2018 September 6; published 2018 October 15

Abstract

Mergers of galaxies are an important mode for galaxy evolution because they serve as an efficient trigger of powerful starbursts. However, observational studies of molecular gas properties during their early stages are scarce. We present interferometric CO(2–1) maps of two luminous infrared galaxies, NGC 3110 and NGC 232, obtained with the Submillimeter Array with ∼1 kpc resolution. While NGC 3110 is a spiral galaxy interacting with a minor (14:1 stellar mass) companion, NGC 232 is interacting with a similarly sized object. We find that such interactions in these galaxies have likely induced enhancements in the molecular gas content and central concentrations, partly at the expense of atomic gas. The obtained molecular gas surface densities in their circumnuclear regions are $\Sigma_{\rm mol} \gtrsim 10^{2.5}\,M_{\odot}\,{\rm pc}^{-2}$, higher than in noninteracting objects by an order of magnitude. Gas depletion times of 0.5–1 Gyr are found for the different regions, lying in between noninteracting disk galaxies and the starburst sequence. In the case of NGC 3110, the spiral arms show on average 0.5 dex shorter depletion times than in the circumnuclear regions if we assume a similar H_2–CO conversion factor. We show that even in the early stages of the interaction with a minor companion, a starburst is formed along the circumnuclear region and spiral arms, where a large population of SSCs is found (∼350), and at the same time a large central gas concentration is building up that might be the fuel for an active galactic nucleus. The main morphological properties of the NGC 3110 system are reproduced by our numerical simulations and allow us to estimate that the current epoch of the interaction is at ∼150 Myr after closest approach.

Key words: galaxies: individual (NGC 3110 – NGC 232) – galaxies: interactions – galaxies: nuclei – galaxies: spirals – galaxies: starburst – ISM: molecules

1. Introduction

Interactions between galaxies are among the most important mechanisms modifying the properties of galaxies through their cosmological lifetime (e.g., Barnes & Hernquist 1992; Springel et al. 2005), especially because the merger rate is seen to be higher in the early universe (e.g., Bridge et al. 2010; López-Sanjuan et al. 2015). Several mechanisms are at play to drive gas from external regions toward the nuclei of galaxies and produce starbursts (SBs) and active galactic nuclei (AGNs). The dissipative nature of the gas leads to a loss of angular momentum in shocks, resulting in subsequent inflows that then trigger SBs within the inner few kiloparsecs of the galaxy, as well as feeding the AGNs (Barnes & Hernquist 1996). Observationally, interactions are seen to play a central role in increasing Star Formation (SF) and concentrating gas toward the center (e.g., Bushouse 1987; Smith et al. 2007; Sabater et al. 2013). Probably the most extreme objects are Ultra/Luminous Infrared Galaxies (U/LIRGs), where IR luminosities are above $10^{11}\,L_{\odot}$, and represent one of the most dramatic phases in galaxy evolution (e.g., Sanders & Mirabel 1996).

The transformation of disk galaxies in the merging process has been widely studied numerically (Toomre & Toomre 1972; Barnes & Hernquist 1992; Mihos et al. 1992; Mihos & Hernquist 1996; Moore et al. 1996; Springel et al. 2005; Cox et al. 2008). Simulations including the stellar and gaseous components of merging systems have covered a wide range of the parameter space, but usually numerical studies presenting the star formation history have focused on major mergers of similarly sized disk galaxies (mass ratios up to 3:1) (e.g.,

Hopkins et al. 2013) rather than galaxies accreting smaller objects. The galaxy mass ratio (together with the closest approach distance and relative velocities) is indeed found to be a major parameter characterizing the resulting merger driven starburst. The induced SF in the primary galaxy for large mass ratio mergers >10:1 is found to be just marginally larger (Cox et al. 2008).

Observationally it is found that there are enhancements of the Star Formation Rate (SFR) especially for galaxy pairs at small projected separations of <30–40 kpc (Ellison et al. 2008), but can be seen up to 150 kpc (Scudder et al. 2012; Patton et al. 2013). These enhancements are larger for galaxies of approximately equal mass, but such an SFR enhancement can also be seen for galaxy pairs whose masses vary by up to a factor of ∼10 (Ellison et al. 2008), although it has been argued that this is true mostly in the least massive galaxy of the pair (Woods & Geller 2007). As for the molecular gas content, from which stars form, Gao & Solomon (1999) found that it decreases as merging advances. Gao & Solomon (1999) also argued that the starburst is probably not due to the formation of more molecular clouds from atomic gas, but enhanced star formation in preexisting molecular clouds. On the other hand, Yamashita et al. (2017) recently found that the molecular gas masses in the central regions of galaxies are relatively constant from early to late merger stages, which they interpreted as molecular gas inflow replenishing the consumed gas by SF. Observations with better resolution are needed in order to probe the detailed properties of molecular gas and onset of SF in these systems.

High angular resolution CO observational studies at different stages of the merging process and for different mass ratios are essential to understand the molecular gas response to the interaction, which have consequences on the subsequent SF activities. A large number of high-resolution observational studies of intermediate to late stage mergers and merger remnants have been performed (Downes & Solomon 1998; Bryant & Scoville 1999; Iono et al. 2005, 2009, 2013; Wilson et al. 2008; Greve et al. 2009; Imanishi et al. 2009; Sliwa et al. 2012; Imanishi & Nakanishi 2013; Ueda et al. 2014; Xu et al. 2014; Saito et al. 2015, 2016, 2017a, 2017b; Sliwa et al. 2017). Although intermediate and late stage major mergers garner a significant fraction of all the observational studies, early stage phases when separations are still relatively large (>40 kpc) have rarely been part of these studies. Therefore, our understanding from an observational point of view of the early stages of the interaction is relatively poor, and it is essential to investigate the impact of smaller objects, as these kinds of events are expected to be more frequent. Although these kinds of systems cannot be easily found locally given the short timescales (a few 10^8 Myr) involved close to the first approach, it is of key importance to complete the sequence of snapshots at every merger stage in order to show how the interstellar medium and SF evolve along the merger process sequence.

In the early stages of a merger, simulations show that galaxies approach each other but are still distinct and the morphology starts to be just slightly distorted. It is established that in this phase the generation of disturbed two-arm barred spirals and tidal bridges/tails occurs (Toomre & Toomre 1972). A direct consequence in this phase of this type of interaction are galactic spiral features (Tutukov & Fedorova 2006; Dobbs et al. 2010), warps (Dubinski & Chakrabarty 2009; Kim et al. 2014), bars (Lang et al. 2014; Pettitt & Wadsley 2018), (stellar and gaseous) bridges that may connect the galaxies, and tidal tails extending well beyond the main body of the galaxies (D'Onghia et al. 2010). Although the tidal interaction forms these kinds of spiral arms and probably relatively long-lived bars, the gas response varies very rapidly and flows efficiently toward the central regions (Iono et al. 2004).

In this paper we present molecular gas maps at ∼1 kpc scale resolution as traced by CO(2–1) for two cases of early stage tidal interactions between galaxies at relatively large distances (≳40 kpc) and with different mass ratios: NGC 3110, interacting with a minor companion of 14:1 its mass, and NGC 232, which is interacting mostly with NGC 235, an object of comparable mass. Our aim is to shed light on the effect that a different galaxy mass ratio has on the molecular gas properties of the primary galaxies and the onset of the starburst in the early stages of the interaction. This paper is organized as follows. First we describe the properties of the two galaxies subject to study in this paper in Section 2. We introduce our Submillimeter Array (SMA) observations and data reduction in Section 3. In Section 4 we focus on the identification of the different molecular components and study their major physical properties. We compare the gas content and SF properties, and derive the spatially resolved SF law in Section 5 with the help of Hα and 24 μm maps. Finally, in Section 6 we compare the observational maps with our own numerical simulations as well as with others in the literature. Our main conclusions are summarized in Section 7. We adopt a cosmology of $\Omega_\Lambda = 0.73$, $\Omega_M = 0.27$, and $H_0 = 73\ \mathrm{km\ s^{-1}\ Mpc^{-1}}$.

2. The LIRGs NGC 3110 and NGC 232

We first summarize the main properties of NGC 3110 and NGC 232, including their morphological properties, environment, activity, and gas properties. The main parameters characterizing these two galaxies are listed in Table 1. Figure 1 shows optical DSS2 and NIR 2MASS composite images, and Figure 2 the Hα maps.

These two objects are part of the SMA B0DEGA project (SMA Below 0 DEgree GAlaxies, Espada et al. 2010), where the CO(2–1) line was observed for about a hundred galaxies with the SMA. Because they are located in the southern sky, most of the galaxies in the sample did not have previous interferometric CO observations published in the literature. The sample is composed of infrared (IR) bright galaxies, selected with the criteria: $2.58 \times S_{60\ \mu\mathrm{m}} + S_{100\ \mu\mathrm{m}} > 31.5$ Jy ($S_{60\ \mu\mathrm{m}}$ and $S_{100\ \mu\mathrm{m}}$ are the *IRAS* 60 and 100 μm fluxes), recession velocities $V < 7000\ \mathrm{km\ s^{-1}}$, and located in the southern sky up to $\delta = -45°$. The galaxies in the sample are mostly of spiral type and members of interacting systems such as groups and pairs of galaxies, but we excluded intermediate and late stage major mergers. The data can be accessed via the CfA SMA database.[19]

NGC 3110 and NGC 232 are the most IR luminous galaxies in the B0DEGA sample, and among the most IR luminous objects that can be found located nearby that are not intermediate/late stage major mergers. Both galaxies were classified as mildly interacting (i.e., separate nuclei, weak tidal features), as opposed to objects with strong tidal features, mergers, and merger remnants (Dopita et al. 2002). These two local LIRGs are also part of the Great Observatories All-Sky LIRG Survey (GOALS, Armus et al. 2009), which is a flux-limited sample ($S_{60\ \mu\mathrm{m}} > 5.24$ Jy) composed of a total of 203 galaxies with $L_{\mathrm{IR}} > 10^{11}\ L_\odot$ based

[19] https://www.cfa.harvard.edu/cgi-bin/sma/smaarch.pl

Table 1
General Properties of NGC 3110 and NGC 232

	NGC 3110	NGC 232
R.A., Decl. [J2000][a]	$10^h04^m02.^s1$, −06° 28′29″	$00^h42^m45.^s8$, −23° 33′41″
T[b]	SB(rs)b pec	SBa(r) pec
Mass ratio with companion	14	0.8
Separation—Velocity difference to companion	38 kpc–235 km s^{-1}	50 kpc–120 km s^{-1}
Nuclear Activity[c]	H II, LIRG	H II, LIRG, LINER
D_{25}, Incl., PA[d]	1.′86, 65°, 171°	0.′97, 47°, 17°
D [Mpc][e]	75.2–352 pc	90.5–420 pc
log(L_B [$L_\odot$])[f]	11.01	10.44
log($M_{H\,I}$ [$M_\odot$])[g]	10.0	9.50
log(M_{mol} [$M_\odot$])[h]	10.37	10.16
M_{mol} /$M_{H\,I}$[i]	2.34	4.57
log(L_{IR} [$L_\odot$])[j]	11.23–11.33	11.30–11.41
SFR [$M_\odot$ yr^{-1}][k]	23.2	27.9
log(SFE [yr^{-1}])[l]	−9.00	−8.71
log($M_\star$ [$M_\odot$])[m]	10.78	10.80

Notes.
[a] Coordinates from NED.
[b] Morphological type following the RC3 system (Barnes et al. 2001).
[c] Nuclear activity type from NED.
[d] Major optical axis, inclination and position angle (N to E) from Hyperleda (Makarov et al. 2014).
[e] Luminosity distance and linear scale from NED using 3K Microwave Background Radiation as reference frame and assuming Ho = 73 km s^{-1} Mpc^{-1}, Ω_{matter} = 0.27, Ω_{vacuum} = 0.73.
[f] log(L_B), base 10 logarithm of the blue luminosity obtained as log(L_B) = 12.192 + 2 log(D) −0.4 × $B_{T,c}$, where $B_{T,c}$ is the apparent B-magnitude corrected by galactic, internal extinction and k-correction, as obtained from Hyperleda.
[g] log ($M_{H\,I}$), base 10 logarithm of the H I masses from Martin et al. (1991), corrected to our choice of distance.
[h] log(M_{mol}), base 10 logarithm of the molecular gas content accounting for elements other than hydrogen. These were calculated from the CO(1–0) integrated intensity measurements in Sanders et al. (1991) for NGC 3110 (12 m NRAO telescope, characterized by a 55″ beam size at 115 GHz) and in Mirabel et al. (1990) for NGC 232 (SEST telescope, 44″ at 115 GHz). We used Jy-to-K conversion factors of 30.4 Jy/K for the 12 m NRAO, and 19 Jy/K for SEST. The X factor is $X = 2 \times 10^{20}$ cm^{-2}(K km s^{-1})$^{-1}$.
[i] $M_{mol}/M_{H\,I}$, molecular to atomic gas fraction.
[j] log(L_{IR}), base 10 logarithm of the 40–400 μm and 8–1000 μm luminosities (in this order) obtained from the four *IRAS* bands 12, 25, 60 and 100 μm, as provided in the Revised Bright Galaxy Catalog (RBGS, Sanders et al. 2003). The value was corrected to our choice of distance.
[k] SFR as obtained from the 8–1000 μm L_{IR} in the previous row (*h*), following SFR = $L_{IR}/(5.8 \times 10^9\ L_\odot)\ M_\odot$ yr^{-1} (as in Equation (3) of Kennicutt 1998b, see also Kennicutt 1998a), and correcting to a Kroupa IMF by a factor 1.59 following Bigiel et al. (2008).
[l] log(SFE = SFR/M_{mol}), base 10 logarithm of the ratio between SFR and M_{mol}.
[m] log($M_\star$), base 10 logarithm of the total stellar mass computed by fitting stellar population synthesis models to the observed near-infrared (NIR) through ultraviolet (UV) SEDs (U et al. 2012; Larson et al. 2016), corrected to our choice of distance.

on the *IRAS* Revised Bright Galaxy Survey (RBGS) presented in Sanders et al. (2003).

2.1. NGC 3110

NGC 3110 is usually classified as a barred Sb galaxy (Table 1). It is located at a distance of D = 75.2 Mpc (1″ corresponds to 352 pc), and it is interacting with a minor companion located to the SW, which likely contributed to the formation of its two asymmetric spiral arms and a central bar-like feature as seen in Figure 1. The optical diameter is 1.′86, or 39.3 kpc. The structure that is usually classified as a bar feature has a length ∼20″ (7 kpc) as seen in Hα emission (Hattori et al. 2004). However, a more careful inspection of high-resolution images reveals that this feature does not resemble the distribution of a standard bar. This galaxy has an overall high SFR of about 20–30 $M_\odot$ yr^{-1}, as obtained from IR and Hα data (Dopita et al. 2002; Yun & Carilli 2002), mostly concentrated toward its center. The SF is fueled by a large mass of molecular gas, estimated to be $M_{mol} \simeq 2 \times 10^{10}\ M_\odot$ (Table 1). There is also abundant SF in the two arms of the galaxy based on Hα maps (Figure 2), with several bright H II knots distributed along them (Dopita et al. 2002; Hattori et al. 2004), and in fact the arms contribute to up to 35% of the FIR flux (Zink et al. 2000). These spiral arms wind up to the center within the inner 9″ (3.2 kpc) as seen in Brγ, H_2 S(1–0), and Fe II in VLT/SINFONI data, and there is also an elongated structure along the N–S direction (Colina et al. 2015). *Hubble Space Telescope* (*HST*) images also show some filaments orienting toward its nuclear region (Malkan et al. 1998). The nuclear activity was classified as H II (Veilleux et al. 1995; Corbett et al. 2003), and so far there is no evidence of AGN in its nucleus.

Following the visual morphological scheme by Larson et al. (2016) for the GOALS sample, from objects in the early stages of interaction to merger remnants, NGC 3110 was classified as an early stage major merger (stage 1, or M1, following their nomenclature), where an early stage major merger is defined as a galaxy pair with a velocity difference between the two galaxies of $\Delta V < 250$ km s^{-1} and separations of less than 75 kpc, which have no prominent tidal features, and appear to be on their initial approach. This classification also implies that the mass ratio between the two interacting galaxies are comparable (<4:1), although the companion of NGC 3110 is likely to be smaller than this. With their morphological classification scheme it would probably fit better into the minor merger case. The companion galaxy is MCG-01-26-013 (PGC029184), which is located at just 1.′8 from NGC 3110, or 38 kpc (Figure 1), and with a (projected) velocity difference of 235 km s^{-1}. Its optical diameter is 0.′98, about half of that of the main galaxy. It is seen nearly edge-on and is classified as S0$^+$pec or S0-a (de Vaucouleurs et al. 1991, Hyperleda). Its (extinction corrected) blue-band luminosity is more than one order of magnitude smaller than that of NGC 3110, $7.3 \times 10^9\ L_\odot$ versus $10^{11}\ L_\odot$ (Table 1), so the mass difference is estimated to be 14:1. There exists Hα emission toward the nucleus of the companion as well, and it is more centrally concentrated than that in NGC 3110 (Dopita et al. 2002). From Very Large Array (VLA) H I observations, it is seen that a local H I minimum is found at the center of NGC 3110, and although the distribution is asymmetric with its peak toward the northern arm, no tidal tail is seen in these maps to a sensitivity of ∼10^{20} atoms cm^{-2} (Thomas et al. 2002).

2.2. NGC 232

At a distance of D = 90.5 Mpc (1″ corresponds to 420 pc), NGC 232 is a barred Sa galaxy seen with an inclination of ∼47° (Table 1), and with two arms that seem to form a ring-like structure in optical images. The size of the disk is 0.′97, or 24 kpc.

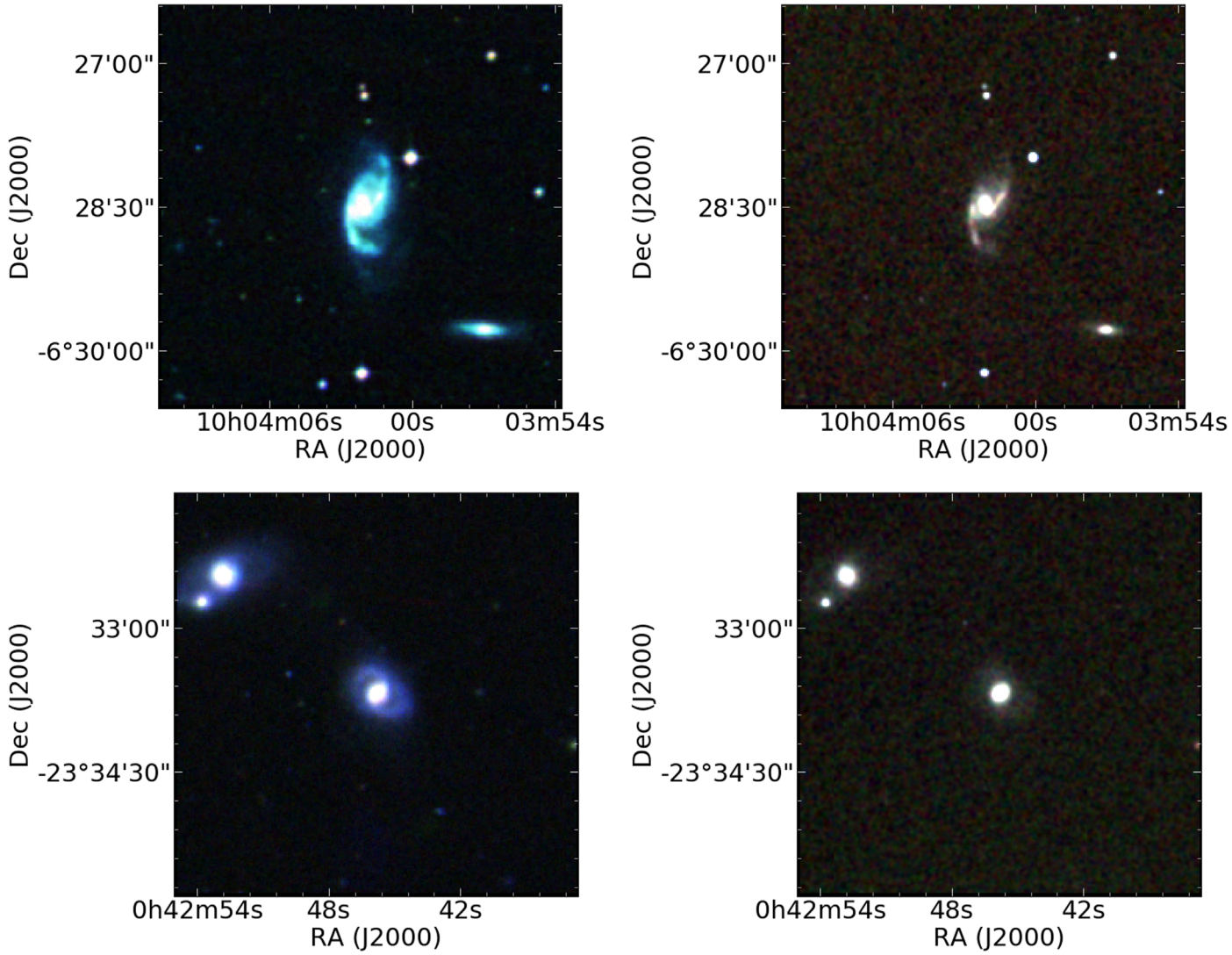

Figure 1. DSS2 blue, IR, red (left) and 2MASS JHK (right) composite RGB images of the NGC 3110 (top) and NGC 232/5 (bottom) pairs. NGC 3110 and NGC 232 are the galaxies in the center of the fields. The size of the maps is 4′.

In the optical image (Figure 1) one can discern that the two spiral arms (to the N and S) are asymmetric and emerge from the barred central component, which is elongated along the SE to NW direction. A high SFR of about 30 $M_{\odot}$ yr^{-1} can be derived from its FIR flux (e.g., Schmitt et al. 2006b). The Hα maps in Schmitt et al. (2006a) show a bright compact nuclear region of about 10″ in diameter elongated along the E–W direction (P.A. $\simeq$ 100°), as well as extended diffuse emission with a somewhat different P.A., which is the direction along the bar-like structure seen in the optical and NIR images at P.A. $\simeq$ 140° (Figure 1), as well as in radio emission (Schmitt et al. 2006a). The brightest component in the Hα map along the E–W direction is also detected in Paα (Tateuchi et al. 2015). The molecular gas mass is estimated to be $M_{\rm mol} \simeq 2 \times 10^{10}\, M_{\odot}$ (Table 1). NGC 232 was classified to host a nuclear starburst (H II) (Veilleux et al. 1995; Corbett et al. 2002), although it has also been classified as a low ionization nuclear emission-line region (LINER) by Coziol et al. (2000). A very extended ($\sim$3 kpc) and highly collimated linear structure extending from the nucleus has been recently found using VLT/MUSE (López-Cobá et al. 2017), which indicates that this is in fact an AGN. This is the second longest optical emission-line jet reported so far.

NGC 232 is classified as a major merger in stage 2, where galaxy pairs show obvious tidal bridges and tails (Larson et al. 2016). Although the companion galaxy to the NE, NGC 235 (ESO 474-G016, Figure 1), might be an evolved merger by itself because it has a double nucleus, the separation to NGC 232 and the lack of disturbed features may indicate that from the point of view of NGC 232 it is in an earlier stage of interaction as well. NGC 235 is a peculiar S0 that is separated by 2′ (or 50 kpc) and with a (projected) velocity difference of $\sim$120 km s^{-1} with respect to NGC 232. Both NGC 232 and 235 are members of a southern compact group of four objects (SCG 10, or SCG 0040-2350, Prandoni et al. 1994; Coziol et al. 2000; Iovino 2002), although we note that two of them are probably merging and are both associated with NGC 235 itself and the fourth is an edge-on spiral galaxy (NGC 230, $V = 6759$ km s^{-1}) to the SW separated by about 5.′9 ($\sim$148 kpc) from NGC 232 and with no signs of interaction. On the other hand, there is a signature of interacting debris between NGC 232 and NGC 235 from the Hα knot that is lying between the two galaxies (Richter et al. 1994; Dopita et al. 2002). These two objects are of comparable size. Assuming the same distance, the blue-band optical luminosities

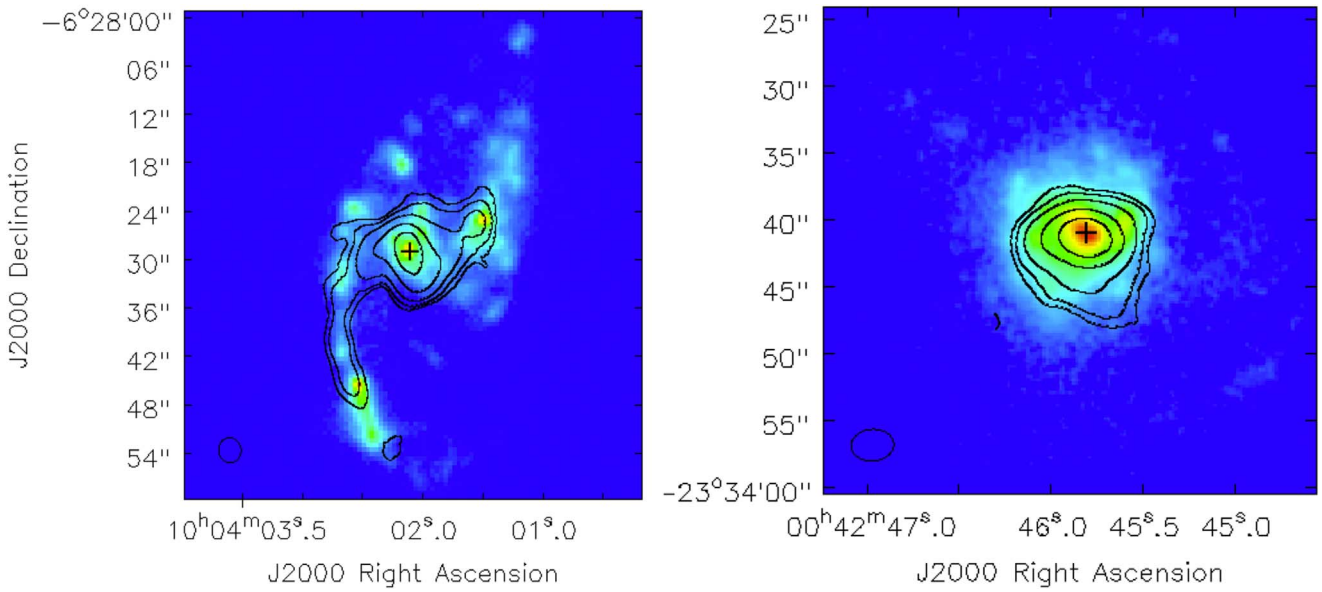

Figure 2. Hα images of NGC 3110 (Hattori et al. 2004) and NGC 232 (Schmitt et al. 2006b) with the SMA CO(2–1) contours overlaid. The field of view is $60'' \times 57''$ and $36'' \times 36''$, respectively. The color scale ranges from 0 to 6.51 10^{-15} erg s^{-1} cm^{-2} and from 0 to 3.85 10^{-15} erg s^{-1} cm^{-2}. The CO(2–1) contours (black) are as in Figures 6 and 7, i.e., at 3, 5, 10, 25, and 50σ, where $\sigma = 1.4$ Jy beam^{-1} km s^{-1} for NGC 3110 and $\sigma = 1.7$ Jy beam^{-1} km s^{-1} for NGC 232. The HPBW of the synthesized beams of the SMA CO(2–1) observations are indicated at the bottom left of the panels. The cross sign shows the center of the galaxies.

for NGC 232 and NGC 235 are $L_B = 2.8 \times 10^{10} L_\odot$ and $3.5 \times 10^{10} L_\odot$. The optical diameters of NGC 232 and NGC 235 are comparable, with that of NGC 235 being slightly larger (24.4 kpc versus 34.8 kpc).

3. Observations and Data Reduction

We present in this paper CO(2–1) observations using the SMA (Ho et al. 2004) toward NGC 3110 and NGC 232. NGC 3110 was observed for 162 minutes (on source) with seven antennas in a compact configuration, with maximum projected baselines of 53.795 kλ, on 2008 October 11, and NGC 232 was observed for 89 minutes (on source) with eight antennas in a slightly more extended configuration with maximum projected baselines of 90.950 kλ, on 2008 May 8 and 21.

Table 2 summarizes the setup of the interferometric observations targeting the CO(2–1) line ($\nu_{\rm rest} = 230.538$ GHz), the calibrators used, as well as the resulting synthesized beams and rms noise levels. The digital correlator was configured with 3072 channels (2 GHz bandwidth), resulting in a velocity resolution of about 1 km s^{-1}. Although the velocity resolution of our CO(2–1) observations is 1 km s^{-1}, we have binned the data cubes to 20 km s^{-1} to have better signal-to-noise ratio (S/N) while still Nyquist sampling the CO(2–1) line. Enough line-free channels are present to subtract the continuum emission. The field of view is characterized by a Half Power Beam Width (HPBW) of the primary beam at 230 GHz of the SMA 6 m antenna of 52″ (18.3 kpc for NGC 3110, and 21.8 kpc for NGC 232), which is sufficient to cover in a single pointing for the whole extent of the two galaxies.

The data were reduced using the SMA-adapted MIR-IDL package.[20] The absolute flux scale for the data was determined by observing one planet or satellite, and quasars were used for the bandpass and the time variable gain corrections (phase and amplitude). By comparing with flux measurements of the phase calibrators close to the time of the observations, we estimate that the absolute flux uncertainty is of the order of 20%.

Table 2
SMA CO(2–1) Observations

	NGC 3110	NGC 232
Date	2008 Oct 11	2008 May 08–21
Time on source	162 minutes	89 minutes
Antennas/Maximum baseline length	7/53.795 m	7/75.573–90.950 m
Field of view	52″ × 52″	52″ × 52″
Beam size	3.″1 × 2.″8	3.″2 × 2.″4
P.A. (N to E)	10.°7	−86.°2
rms noise channel 20 km s^{-1} [mJy/beam]	14	15
Calibrators (ampl./bandpass/phase (separation))	3C84/3C84/1058+015 (15.°8)	Uranus/3C454.3/2258-279 (23.°9)

The imaging of the CO(2–1) line was conducted in MIRIAD (Sault et al. 1995). The continuum was fit with a constant offset from all the line-free channels with the task `UVLIN` and subtracted from the line. The data were `INVERT`ed using `ROBUST` = 0.5. For NGC 3110 the obtained synthesized beam is 3.″1 × 2.″8 (or 1.1 × 1.0 kpc) with a major axis of P.A. = 10.°7 (east of north). The rms noise level is 14 mJy beam^{-1} for a 20 km s^{-1} channel. As for NGC 232, the resulting synthesized beam is 3.″2 × 2.″4 (or 1.3 × 1.0 kpc) with a major axis of P.A. = −86.°2. The rms noise level is found to be 15 mJy beam^{-1} for a 20 km s^{-1} channel.

The dirty images were then deconvolved with the task `CLEAN`. First we carried out the deconvolution without any

[20] MIR is a software package to reduce SMA data based on the package originally developed by Nick Scoville at Caltech. See https://www.cfa.harvard.edu/~cqi/mircook.html.

supporting region for each channel. We created a mask with regions where emission was apparent, which were selected to be large enough (at least ∼10″ diameter) not to miss any possible extended emission. The regions were refined manually in several iterations and the effectiveness of the selection was assessed by minimizing the noise level in line-free regions of the channels, as well as reducing the contribution by sidelobes. The stopping criteria was a clean cutoff limit, 14 mJy beam^{-1} for NGC 3110 and 15 mJy beam^{-1} for NGC 232. The cumulative fluxes as a function of number of clean components were seen to converge in all channels. We considered other less restrictive cutoff limits but they were seen not to converge in channels with more complex distribution. The number of clean components ranged from ∼200 (in the channels corresponding to the edges of the profiles) to ∼800 in the case of NGC 3110, and ∼200–400 for NGC 232. The final residual channel images looked like noise in all channels.

4. Results

In this section we present the results obtained from the SMA CO(2–1) data, including spectra, channel and moment maps, as well as position–velocity (P–V) diagrams.

4.1. CO(2–1) Profiles and Recovered Flux

In Figure 3 we present the CO(2–1) spectra of both galaxies integrated over the area with detected emission within the HPBW of 52″ at 230 GHz. Note that throughout this paper radial velocities are expressed in the radio definition and with respect to the Local Standard of Rest (LSRK frame). The CO(2–1) profiles of both objects are relatively flat. In the case of NGC 3110, we can slightly discern a double peak, at 4900 and 5120 km s^{-1}, the approaching side being brighter than the opposite one. Emission is detected from 4780 to 5240 km s^{-1} in NGC 3110, and from 6370 to 6970 km s^{-1} in NGC 232. The velocity widths are then $\Delta V = 460 \pm 10$ km s^{-1} and 600 ± 10 km s^{-1}, and if corrected by inclination (65° and 47°, Table 1), $\Delta V_{\rm corr} = 508$ km s^{-1} and 820 km s^{-1}, respectively. The systemic velocities obtained from the average of the profile edges at a 20% level of the peak are 4990 ± 10 km s^{-1} and 6650 ± 10 km s^{-1} for NGC 3110 and NGC 232, respectively. The systemic values are consistent with those in the literature if we correct the offsets due to the different velocity frame conventions.

To quantify how much flux is recovered by our interferometric observations, we compare the flux with previously obtained single-dish CO(2–1) data. The total SMA CO(2–1) flux measurements for NGC 3110 and NGC 232 corrected by the primary beam response are 679 and 295 Jy km s^{-1}, respectively. Unfortunately no CO(2–1) single-dish data could be found in the literature for NGC 3110. We use for this comparison the CO(1–0) single-dish integrated flux of 395 Jy km s^{-1} obtained from the NRAO 12 m spectrum presented in Sanders et al. (1991), with a 55″ HPBW, which almost matches the SMA field of view, and we assume a Jy-to-K conversion factor of 30.4 Jy/K. We then convert to the CO(2–1) integrated flux by assuming that the integrated intensity ratio between CO(2–1) and CO(1–0) (in Tmb scale) is $R_{2-1/1-0} \sim 0.8$. This is reasonable because the line intensity ratio $R_{3-2/1-0}$ within the inner 14.″5 is $R_{3-2/1-0} = 0.78$ (Yao et al. 2003). Assuming $R_{2-1/1-0} = 0.8$, the CO(2–1) total flux yields 1264 Jy km s^{-1}, and although with large uncertainties due to the various assumptions, we estimate that the recovered flux in our experiment is ∼54%. The comparison for NGC 232 is more straightforward because a direct CO(2–1) flux measurement exists in the literature. The CO(2–1) integrated intensity (in $T_{\rm mb}$ scale) obtained using the SEST telescope is 17.8 K km s^{-1} with a beam of 23″ (Chini et al. 1996; Albrecht et al. 2007). Given the compact CO(2–1) distribution seen in the SMA maps, as well as in the Hα maps, it is reasonable to think that most of the emission will arise well within the SEST beam. The total flux is then 409 Jy km s^{-1} assuming a 23 Jy/K conversion factor. We thus estimate that ∼70% of the flux is recovered.

We also tested the existence of missing flux in the SMA data by tapering visibilities to increase the brightness sensitivities. We found that for NGC 3110 a taper resulting in angular resolutions of 5″ (and 7″) increase the total integrated flux by 7 %. Flux loss was found to be up to ∼20% in some channels ± 100 km s^{-1} of the systemic velocity where there is more complex distribution. This effect was not noticeable at channels corresponding to the profile edges as a result of the more compact distribution there. As for NGC 232, no clear difference in total integrated flux was found for tapers at 5″ and 7″.

4.2. CO(2–1) Interferometric Maps

Figure 4 shows the CO(2–1) channel maps of NGC 3110. The CO(2–1) channel maps show blueshifted (approaching) emission on the N and redshifted (receding) emission on the S. We distinguish in these maps an inner circumnuclear component within ∼10″ in diameter (3.5 kpc), which is the fastest rotating feature. A more extended component is composed of two main spiral arms which wind up and are linked to the circumnuclear feature. Figure 5 shows the CO(2–1) channel maps of NGC 232. The maps show a compact, although resolved, disk-like structure with blueshifted emission on the NE and redshifted on the SW.

The task `IMMOMENT` in CASA (McMullin et al. 2007) was used to calculate the integrated intensity maps, intensity-weighted velocity fields, and velocity dispersion distributions. We applied masks to each channel as in the deconvolution process. The latter two moment maps were clipped at 2 and 3 times the rms noise for NGC 3110 and NGC 232, respectively. Note that no primary beam correction was performed in the presented integrated intensity map. The moment maps for NGC 3110 and NGC 232 are displayed in Figures 6 and 7, respectively. In Figure 2 we show the same CO(2–1) moment 0 contours over the Hα maps. There is a large concentration of molecular gas toward the inner few kiloparsecs of these two galaxies. The concentration width scale (σ) obtained from a Gaussian fit on the azimuthally averaged intensity radial profile is found to be 1.4 and 0.8 kpc, comparable to the resolution element, and at 1/e level with respect to the central peak the CO scale length is 2.8 kpc and 1.7 kpc, respectively. The radial profiles are shown in Figure 3 (bottom).

The CO(2–1) moment 0 map of NGC 3110 in Figure 6 reveals the whole extent and morphology of the two asymmetric molecular spiral arms, one to the S and a relatively weaker and shorter one to the N, which wind up into the circumnuclear molecular gas component. The circumnuclear component is elongated and extends about 10″ diameter in the

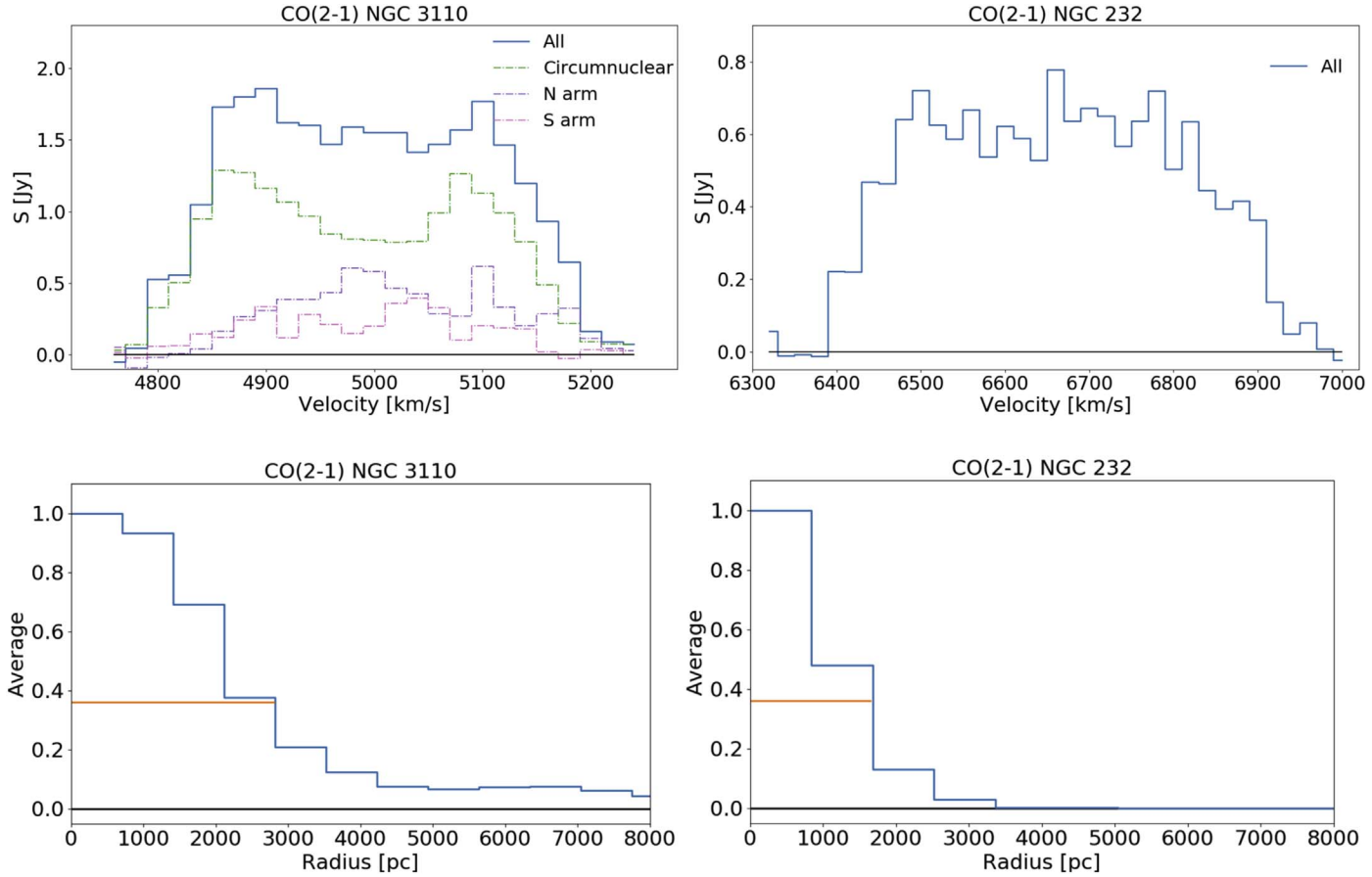

Figure 3. (Top) CO(2–1) spectra for NGC 3110 and NGC 232. The *y*-axis shows fluxes in units of Jy and the *x*-axis the radio LSRK velocities in bins of 20 km s^{-1}, as in the channel maps (Figures 4 and 5 for each galaxy). For NGC 3110 (top left panel), dashed–dotted lines correspond to the circumnuclear region (green), the northern (purple), and southern (pink) arms. (Bottom) The azimuthally averaged CO(2–1) normalized radial profiles for NGC 3110 (left panel) and NGC 232 (right). The *x*-axis shows the radius from the center of the galaxies up to 8 kpc and is expressed in pc. The horizontal (red) line shows the width at 1/e of the central peak.

NE to SW direction. The southern arm is on the receding side of the galaxy, emerging to the E of the central component and extending up to 26″ (9.2 kpc) from the nucleus. The northern molecular arm emerging from the W of the central component is, on the other hand, much shorter, 18″ (6.3 kpc) from the nucleus, and its opening angle differs from that of the southern counterpart. The southern arm is particularly narrow and it is barely resolved in the perpendicular direction with the SMA data. The northern arm is more asymmetrically distributed and appears to be wider than the southern arm.

The CO emission of NGC 3110 peaks very close to the center of the galaxy, but the kinematic center as seen from the CO(2–1) maps is offset by about 1″ to the SE. This central component is characterized by the largest velocity gradient, as seen in the velocity dispersion map in Figure 6, with typical values of 40 km s^{-1} within the inner 5″ (1.8 kpc) (as opposed to the 10–20 km s^{-1} found along the spiral arms) and even $\geqslant$80 km s^{-1} in the central 3″ × 7″ along the E–W direction. The circumnuclear molecular gas component in the inner few kiloparsecs has a P.A. $\simeq$ 10°. This component is aligned with the brightest nuclear barred feature seen in optical/NIR emission (see Section 2.1). The velocity width at zero intensity is the largest, $\Delta V = 460$ km s^{-1}, along this direction and the size of the circumnuclear component is about 10″ × 3″ (3.5 × 1.1 kpc). Noncircular motions (and/or warp) within the circumnuclear component are clear as seen from the twisted morphology in the moment 1 map. The second brightest component in the CO(2–1) map is part of the northern arm, at a distance of 9″ (3.2 kpc) to the NW from the center. It has a relatively symmetric counterpart in the southern spiral arm as seen in the channels 5020–5040 km s^{-1} in Figure 4, although not as bright.

The CO(2–1) maps of NGC 232 show that most of the emission is centrally concentrated within the inner 6″ (2.5 kpc), which we will refer to as the circumnuclear disk, although there is a more extended component of size ∼10″ (4.2 kpc), slightly elongated along the SW–NE direction. It is well-centered on the brightest nuclear component as seen in optical and NIR images. The P.A. of the kinematical axis of the inner portion is about 35° different to that of the most extended component, and is almost perpendicular to the axis of the putative bar at P.A. = 140° (see Section 2.2). To our sensitivity limit we do not detect molecular gas external to the circumnuclear component in the form of spiral arms. An S-shape morphology is also seen in the velocity field (Figure 7), which may suggest either noncircular motions or a warp. This, together with the nearly perpendicular barred-like feature seen in the optical/NIR images, indicates that the circumnuclear disk may represent the family of x_2 orbits in a bar potential. The moment 2 map (Figure 7) shows large velocity dispersions within the circumnuclear disk up to 130 km s^{-1}. The CO(2–1) profile is very wide, 600 km s^{-1} (or 820 km s^{-1} if corrected by

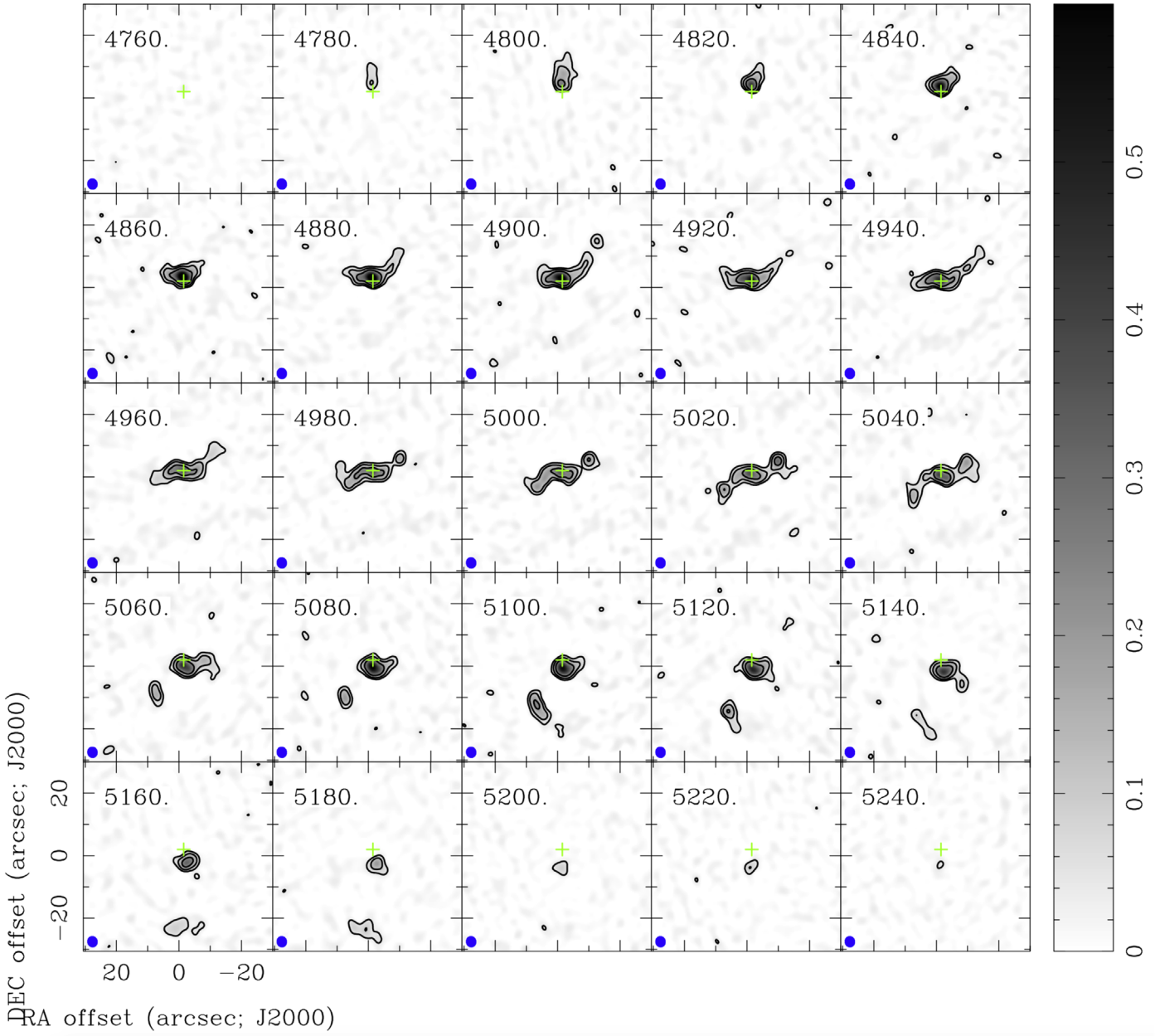

Figure 4. CO(2–1) channel maps of NGC 3110 in the velocity range 4760–5240 km s^{-1} (radio LSRK) in 20 km s^{-1} bins. The size of the maps is 52″. The velocities are shown in the upper right corner of each panel and the synthesized beam is shown in the bottom left corner. The rms noise of an individual channel is $\sigma = 0.014$ Jy beam^{-1}. The contour levels are at 3, 7, and 14σ. The gray scale ranges from 0 to 0.6 Jy/beam. The cross sign shows the center of the galaxy.

inclination) at full-width zero intensity, which is difficult to explain simply by noncircular motions. The emission corresponding to the wings of the spectrum ($V < 6460$ km s^{-1} and $V > 6900$ km s^{-1}) are distributed along a P.A. = 44° (see the high velocity component contour maps in the moment 0 panel of Figure 7), and we speculate that it might be an outflowing component. Follow-up observations with higher angular resolutions are needed to confirm this.

Finally, position–velocity (P–V) diagrams are shown in Figure 8 for NGC 3110 and in Figure 9 for NGC 232. Figures 8 (a) and (b) show P–V cuts along P.A. = 166° and perpendicular to it, 76°, both centered at NGC 3110's nucleus. The slope in the central molecular component is $\Delta V/\Delta r \simeq 0.15$ km s^{-1} pc^{-1}, as opposed to the slower rotation of the external CO components associated with the spiral arms. Note that one can see a distinct component with a smaller slope on the left side of the P.A. = 166° P–V diagram that corresponds to the southern arm. Figure 9 shows the P–V cut along P.A. = 44° of NGC 232. The slope is steeper in this case, $\Delta V/\Delta r \simeq 0.4$ km s^{-1} pc^{-1}. Note that beam smearing due to the relatively coarse spatial resolution likely makes the velocities of these curves lower limits.

4.3. Molecular Gas Mass

First, we obtain the CO(2–1) luminosity, given by $L_{\rm CO(2-1)} = (c^2/2k_B) S_{\rm CO(2-1)}\ \nu_{\rm obs}^{-2}\ D_{\rm L}^2$, where c is the light speed, k_B is the Boltzmann constant, $S_{\rm CO(2-1)}$ is the integrated CO(2–1) line flux in Jy km s^{-1}, $\nu_{\rm obs}$ is the observed rest frequency in GHz,

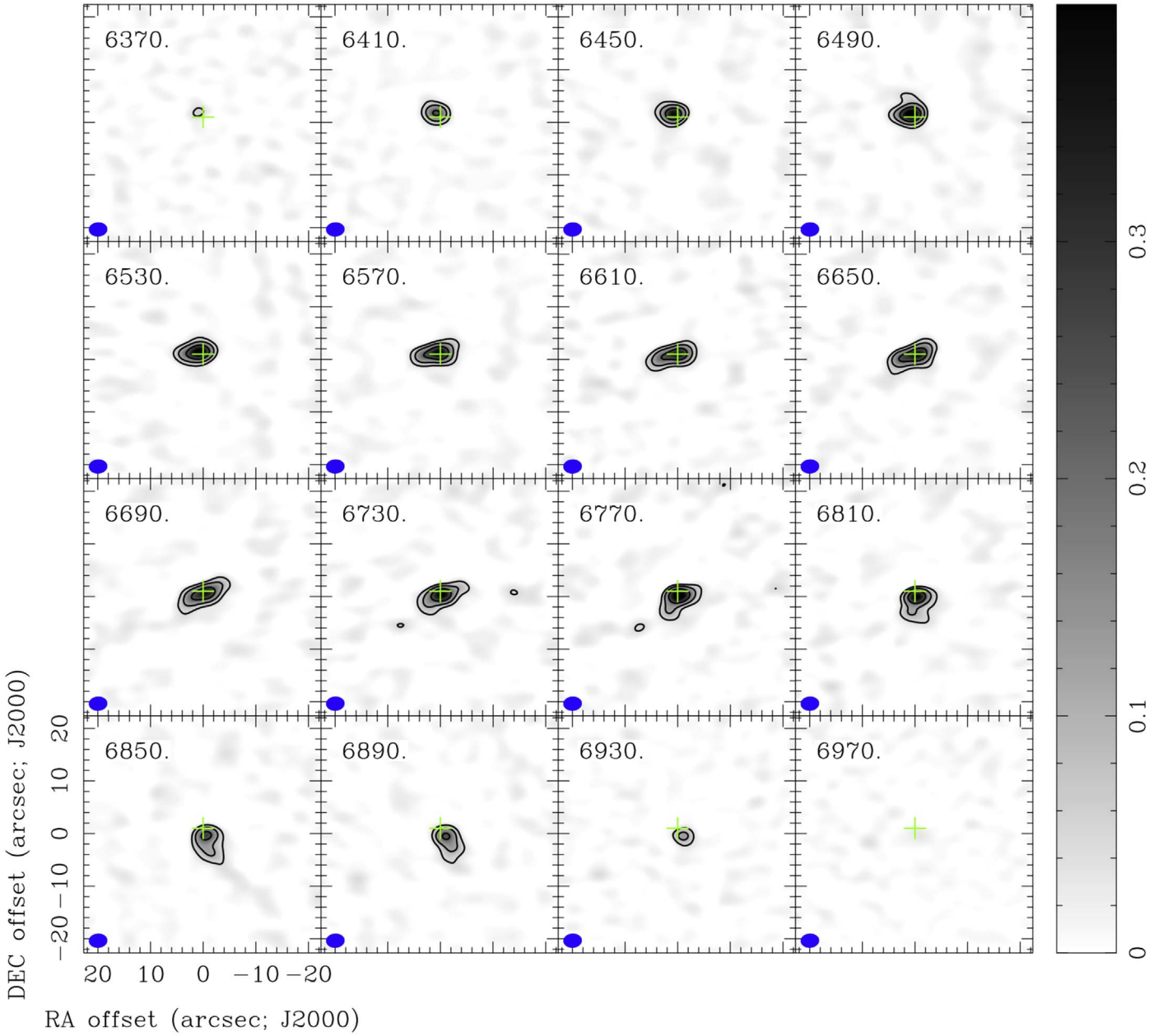

Figure 5. CO(2–1) channel maps of NGC 232 in the velocity range 6370–6970 km s^{-1} (radio LSRK) in 40 km s^{-1} bins. The size of the maps is 45″. The velocities are shown in the upper right corner of each panel and the synthesized beam is shown in the bottom left corner. The rms noise of an individual channel is $\sigma = 0.011$ Jy beam^{-1}. The contour levels are at 3, 7, and 14σ. The gray scale ranges from 0 to 0.4 Jy/beam. The cross sign shows the center of the galaxy.

230.538 GHz, and D_L is the luminosity distance to the source in Mpc (e.g., Solomon & Vanden Bout 2005). It yields $L_{CO(2-1)} = 611 \times S_{CO(2-1)}\, D_L^2$ [K km s^{-1} pc^2]. We use a conversion factor between the CO integrated intensity and H_2 column density of $X_{CO} = N_{H_2}/I_{CO} = 2.0 \times 10^{20}$ cm^{-2} (K km s^{-1})$^{-1}$. This value is recommended for our Milky Way (e.g., Dame et al. 2001) and "normal" (i.e., non-starbursting) galaxies (Bolatto et al. 2013). A caveat is that lower X_{CO} can be present in starburst systems (Yao et al. 2003; Papadopoulos et al. 2012; Bolatto et al. 2013), but the scatter found in these systems is large and it is not clear what the appropriate value might be for these two objects under study. We use for NGC 3110 the integrated intensity CO(1–0) to CO(2–1) line ratio $R_{2-1/1-0} = 0.8$ (see Section 4.1), and for NGC 232 $R_{2-1/1-0} = 0.46$, as calculated from IRAM 30 m CO(1–0) and SEST CO(2–1) observations (Chini et al. 1996; Albrecht et al. 2007), where the calculated integrated intensities (in Tmb scale) were 38.2 K km s^{-1} and 17.8 K km s^{-1}, respectively.

Finally, we calculate the molecular gas masses as $M_{mol}[M_\odot] = 4.3 \times X_2\ (R_{2-1/1-0})^{-1} L_{CO(2-1)}$ (Bolatto et al. 2013), where the factor 1.36 for elements other than hydrogen (Cox 2000) is taken into account, and X_2 is the X_{CO} factor normalized to 2×10^{20} cm^{-2} (K km s^{-1})$^{-1}$. Table 3 shows the derived parameters of the different molecular gas components (i.e., circumnuclear region, NE and SW arms in NGC 3110, and circumnuclear region in NGC 232). The parameters include the velocity ranges, total CO(2–1) integrated fluxes

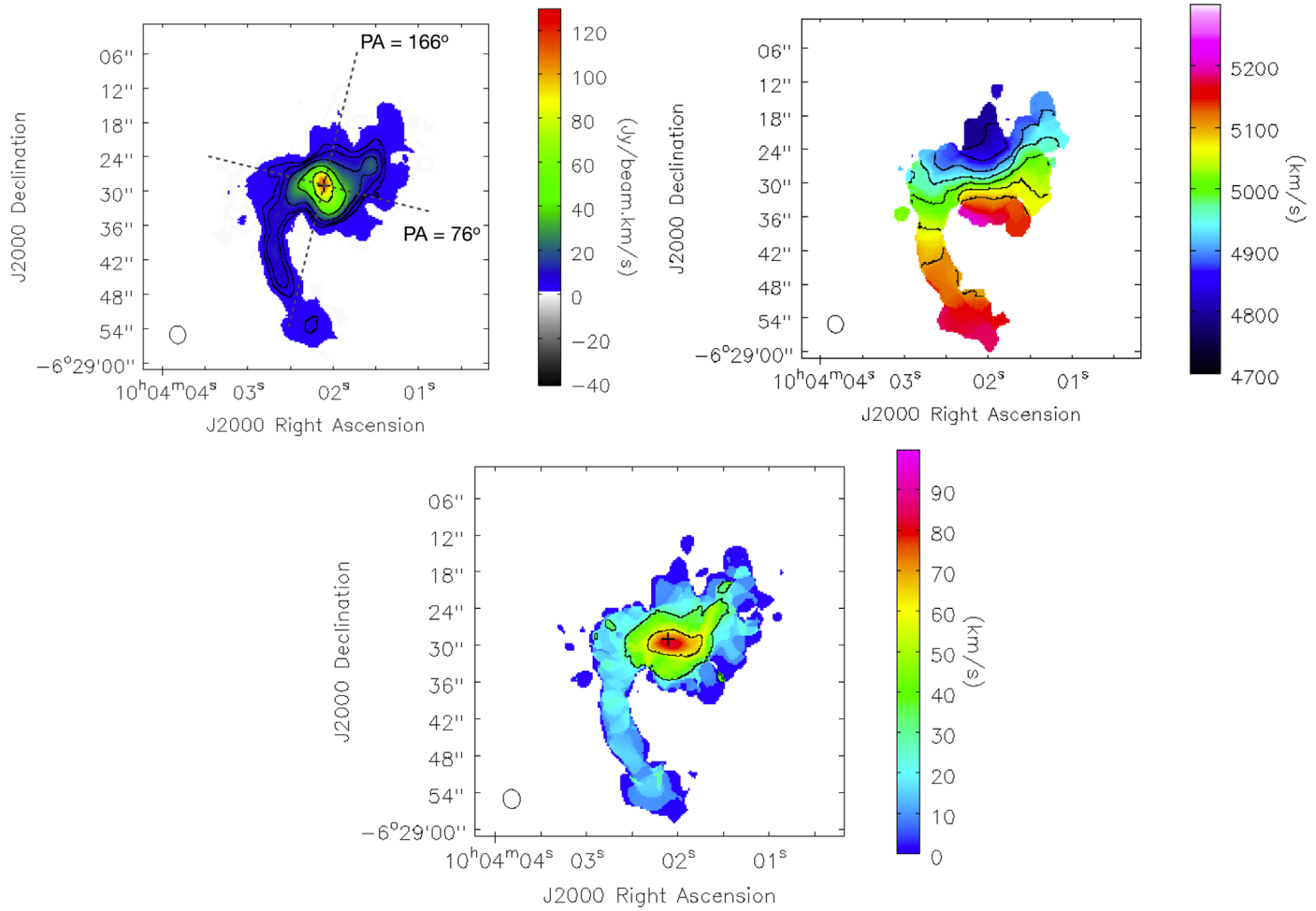

Figure 6. Integrated intensity map (upper left), the intensity-weighted velocity field (upper right), and the intensity-weighted velocity dispersion map (bottom) of NGC 3110. The color scale is shown on the right side of each panel and the HPBW of the synthesized beam ($3\farcs1 \times 2\farcs8$) is indicated as an ellipse at the bottom left. The cross sign indicates the center of the galaxy. Contour levels in the integrated intensity map are at 3, 5, 10, 25, and 50σ, where $\sigma = 1.4$ Jy beam^{-1} km s^{-1}. Contour levels in the velocity field are from 4750 to 5100 km s^{-1} in bins of 50 km s^{-1}. Contour levels in the velocity dispersion map range from 0 to 100 km s^{-1} in 30 km s^{-1} bins. The dashed lines in the moment 0 panel indicate the cuts for the two position–velocity diagrams in Figure 8.

for each galaxy and component, and the derived molecular gas masses. Both galaxies have molecular gas masses of about (1–2) $\times$ 10^{10} $M_{\odot}$, and these are consistent (if corrected by flux losses) with previously reported values.

4.4. Molecular Gas Concentration and Gas-to-dynamical Mass Ratios

Two mechanisms are usually invoked to explain how gas is driven to the circumnuclear regions of galaxies: interactions between galaxies and barred potentials. First, we calculate the molecular gas concentration (see Table 4) to see whether the two interacting objects studied in this paper have comparable concentrations to those in literature samples of noninteracting or weakly interacting barred and unbarred galaxies.

The molecular gas concentration is on the high side when compared to noninteracting and non-barred objects, although not as high as in some barred galaxies. Within a radius of $\sim$1 kpc (i.e., in the inner resolution element), the molecular gas surface densities (in the plane of the disk) are $\Sigma_{\rm mol}^{\rm 1\,kpc} = 306$ and 455 $M_{\odot}$ pc^{-2} for NGC 3110 and NGC 232 (see Section 5.4). We note that within the inner regions, uncertainties due to flux loss are expected to be small (Section 4.1). The concentration factor of molecular gas, defined as $f_{\rm con} = \Sigma_{\rm mol}^{\rm 1\,kpc}/\Sigma_{\rm mol}^{\rm disk}$, where $\Sigma_{\rm mol}^{\rm disk}$ is the disk surface density within the optical radius R_{25} (isophotal radius at 25 mag arcsec^{-2} in B-band) obtained from the total molecular gas content obtained with the single-dish measurements (thus not affected by flux loss), is 38 for NGC 3110 and 22 for NGC 232. These values for $f_{\rm con}$ are likely upper limits in case there is some flux loss in the 1 kpc measurement, and also because it is expected that the molecular gas distributions are not homogeneous within the inner 1 kpc radius. Sakamoto et al. (1999) found that on average unbarred galaxies present a degree of concentration a factor of four times lower than barred systems. They measured $f_{\rm con}$ (defined with respect to a radius of 500 pc) to be 100.2 $\pm$ 69.8 (the error is the standard deviation, for 10 objects) and 24.9 $\pm$ 18.5 (10 objects) for non-barred objects. We note that in the case that $X_{\rm CO}$ is smaller in the circumnuclear regions than in the outer disk, $f_{\rm con}$ will decrease. However, Sakamoto et al. (1999) used a constant $X_{\rm CO}$ factor across galaxies and for different radii, so we can directly compare. The limitation is that we need to estimate the gas surface densities within a 500 pc radius, $\Sigma_{\rm mol}^{\rm 500pc}$, which correspond to a size smaller than our resolution element. It is reasonable to expect that the CO(2–1) distributions of the two galaxies in this paper are centrally concentrated within 1″ by comparing with the structures seen in other ISM

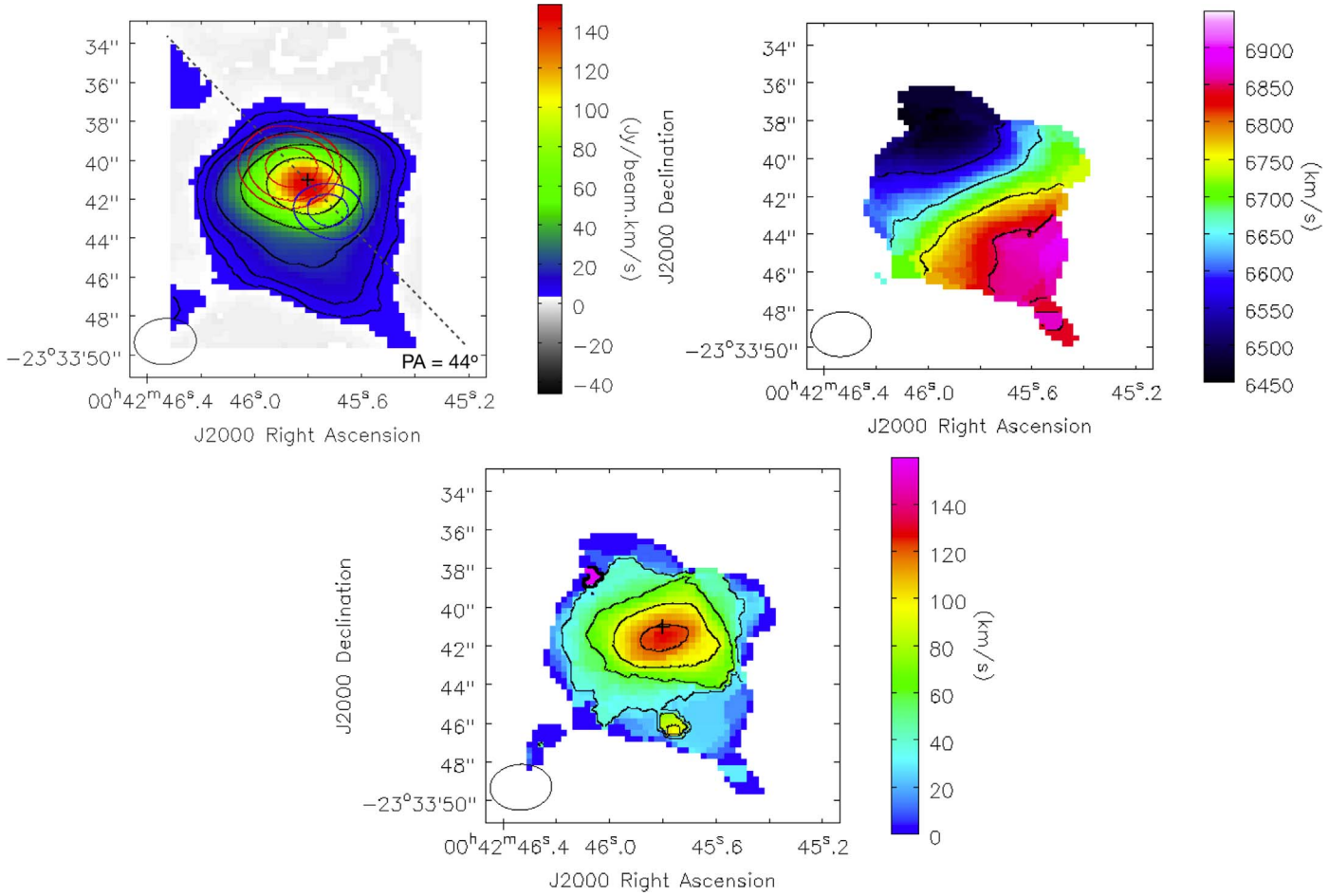

Figure 7. Integrated intensity map (upper left), the intensity-weighted velocity field (upper right), and the intensity-weighted velocity dispersion map (bottom) of NGC 232. The color scale is shown on the right side of each panel and the HPBW of the synthesized beam ($3\farcs2 \times 2\farcs4$) at the bottom left. The cross sign indicates the center of the galaxy. Contour levels in the integrated intensity map are at 3, 5, 10, 25, and 50σ, where $\sigma = 1.7$ Jy beam^{-1} km s^{-1}. Contours for the approaching (blue, $V < 6460$ km s^{-1}) and receding (red, $V > 6900$ km s^{-1}) wings of the profile are also shown. The contour levels for the approaching contours are 3, 5, and 10σ, and for the receding ones 3 and 5σ. Contour levels in the velocity field are 6550, 6650, 6750, and 6850 km s^{-1}. Contour levels in the velocity dispersion map range from 0 to 120 km s^{-1} in 30 km s^{-1} intervals. The dashed line in the moment 0 panel indicate the cut for the position–velocity diagram in Figure 9.

components (see for example H_2 1–0 S(1) and ionized emission for NGC 3110 in Colina et al. 2015). We estimate that $\Sigma_{\rm mol}^{\rm 500pc}$, and therefore $f_{\rm con}$, will then increase by a factor of 50%, which will result in concentrations closer to the typical value of barred galaxies, or at the high end of non-barred objects. It is thus likely that a large amount of gas is transported to the circumnuclear regions due to the interaction itself, and at least in the case of NGC 3110, prior to the formation of a bar. The $f_{\rm con}$ values estimated here should be confirmed in the future with better angular resolution CO data.

Next, we estimated the gas-to-dynamical mass ratio within a radius of 1 kpc ($f_{\rm dyn}$, see Table 4), which is closely related to the stability of the disk. The dynamical masses within 1 kpc are derived from equation $M_{\rm dyn} = r\ (V/\sin(i))^2/G$, where r is radius in pc, V the rotational velocity (230 km s^{-1} for NGC 3110 and 300 km s^{-1} for NGC 232, see Section 4.2), i the inclination, and G the gravitational constant. The gas-to-dynamical mass ratios we obtain, $f_{\rm dyn} = 0.06$ for NGC 3110 and 0.03 for NGC 232, are comparable to the values found in other galaxies, which for a radius of 500 pc, $f_{\rm dyn} = 0.01$–0.3 (e.g., Sakamoto et al. 1999; Martín et al. 2010). Within the inner 1 kpc, uncertainties due to flux loss are expected to be small (Section 4.1), so we do not expect that this issue will considerably affect the $f_{\rm dyn}$ measurements.

5. Properties of the Interaction, Conversion from H I to H_2 and Resulting Star Formation

5.1. Properties of the Interacting Systems

From the relatively small separations and velocity differences, one can infer that it is likely that the two galaxies and their companions are probably gravitationally bound based on escape velocity arguments. However, the separations and velocity differences are just projected values along the line of sight so it is difficult to discard the fly-by hypothesis. From the lack of strongly perturbed morphologies and tidal tails in the stellar, ionized, and (molecular) gas components, it is reasonable to expect that the interaction is in an early stage. This is backed up by simulations (e.g., Mihos & Hernquist 1996; Iono et al. 2004). The H I observations for NGC 3110 reinforce this idea because of the lack of H I tidal tails in the VLA H I maps presented in Thomas et al. (2002), at least to a sensitivity of about 10^{20} atoms cm^{-2}. However, the VLA H I integrated flux is $S_{\rm H\,I,VLA} = 2.9 \pm 0.9$ Jy km s^{-1}, and the Nancay single-dish measurement $S_{\rm H\,I,Nancay} = 7.6$ Jy km s^{-1} (Martin et al. 1991), which shows that the interferometric experiment is likely affected by missing flux due to a lack of zero spacings. No high-resolution H I map exists for NGC 232 to our knowledge. H I spectral asymmetries can also be a way to probe the level of

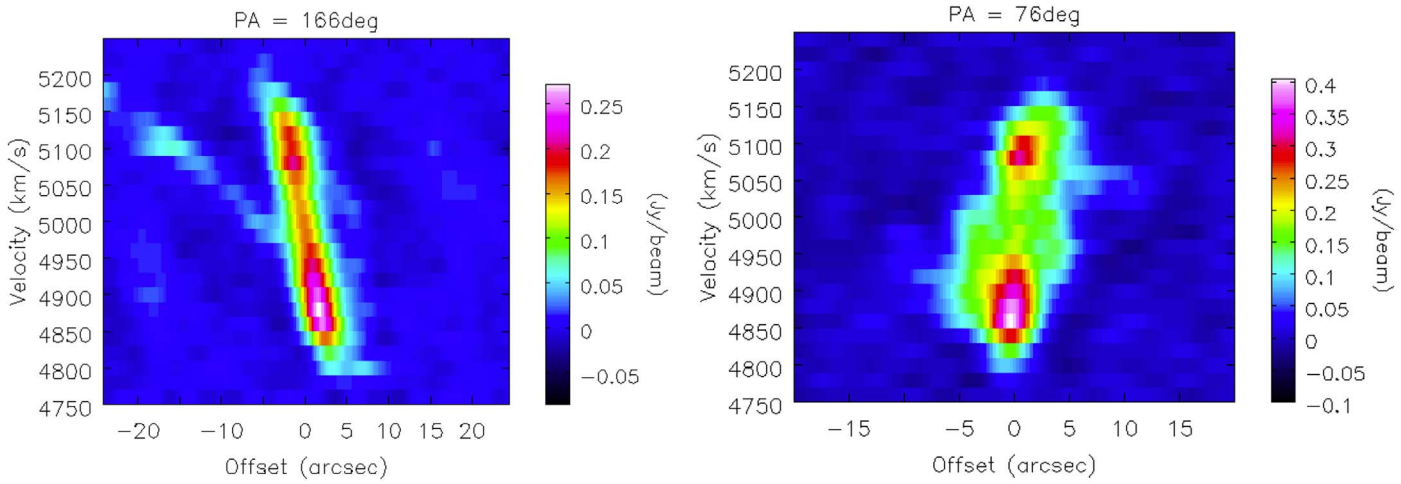

Figure 8. CO(2–1) Position–Velocity (P–V) diagrams of NGC 3110: (left) at PA = +166°, length of 50″, and averaging width 16″, (right) at PA = 76°, length of 40″, and averaging width of 7″. The color scales are shown on the right side of each panel.

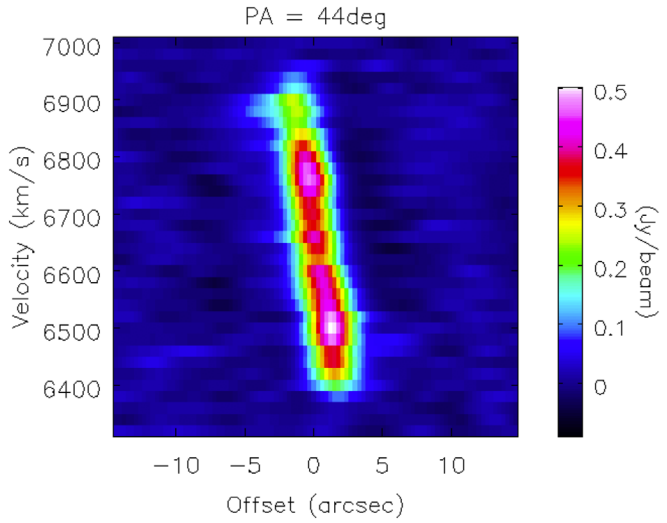

Figure 9. CO(2–1) Position–Velocity (P–V) diagram of NGC 232 for a cut at PA = 44°, length of 30″, and averaging width of 5″. The color scale is shown on the right side.

interaction (Espada et al. 2011). The H I profile of NGC 3110 in Martin et al. (1991) is two peaked and relatively symmetric, but may reveal a small wing in the redshifted edge of the profile (which is to the north of the galaxy), and the H I line of NGC 232 also shows a peculiar profile with three peaks, although the S/N is relatively poor.

Next, we quantify the tidal strength of the interactions. The local tidal force exerted by the companion galaxy (B) on the main galaxy (A) can be estimated from the following equation:

$$Q_{\rm pair} = \log\left(\frac{M_B}{M_A}\left(\frac{D_A}{d_{AB}}\right)^3\right), \quad (1)$$

where M_X is the stellar mass of X = A or B, D_A is the estimated diameter of galaxy A, and d_{AB} is the projected physical distance between the two galaxies (Verley et al. 2007; Argudo-Fernández et al. 2014, 2015). Since the luminosity is proportional to mass, we use the B-band luminosity ratio in this calculation. The tidal strengths are $Q_{\rm pair} = -1.1$ and -0.85 for NGC 3110 and NGC 232, respectively. Clearly the tidal strength for NGC 232 is greater than that of NGC 3110. Indeed, the interacting galaxies in the NGC 232 pair are closer and the masses are comparable. These values of $Q_{\rm pair}$ for the two objects are, just by the contribution of their corresponding companions, much greater than those in galaxies considered to be mostly isolated (Verley et al. 2007; Argudo-Fernández et al. 2013), and when compared to isolated pairs, we see that they are at the high end of the distribution, so these two interactions are generally stronger. The mean and standard deviation for a sample of isolated galaxies are $Q_{\rm isolated} = -5.19$ and $\sigma_{Q,\rm isolated} = 0.84$, and for isolated pairs $Q_{\rm pair} = -2.27$ and $\sigma_{Q,\rm pair} = 1.24$ (Argudo-Fernández et al. 2015).

Table 3
Derived Parameters of the Different Regions Detected in CO(2–1)

Component	Velocity Range (km s^{-1})	$S_{\rm CO(2-1)}$[b] (Jy km s^{-1})	$M_{\rm mol}$[c] ($M_\odot$)
NGC 3110			
Spiral arm NW	4800–5140	116	(2.1–3.9) × 10^9
Spiral arm SE	4860–5200	165	(3.1–5.7) × 10^9
Circumnuclear region[a]	4780–5240	358	(6.6–12.2) × 10^9
All	4760–5240	679	(1.3–2.4) × 10^{10}
NGC 232			
All	6370–6970	295	(1.4–2.0) × 10^{10}

Notes.
[a] The circumnuclear region of NGC 3110 is defined as the region within an ellipse with major axes 12.″4 × 8.″0 (4.6 kpc × 2.9 kpc), centered at its nucleus and with P.A. = 0°.
[b] Integrated CO(2–1) flux, corrected by primary beam but not by flux loss.
[c] $M_{\rm mol}$, the molecular gas mass, is calculated as $M_{\rm mol}[M_\odot] = 4.3 \times X_2\,(R_{2-1/1-0})^{-1} L_{\rm CO(2-1)}$, where the CO(2–1) luminosity is derived as $L_{\rm CO(2-1)} = 611 \times S_{\rm CO(2-1)}\, D_{\rm L}^2$ [K km s^{-1} pc^2]. The factor 1.36 for elements other than hydrogen (Cox 2000) is taken into account, X_2 (i.e., X factor normalized to 2 × 10^{20} cm^{-2} (K km s^{-1})$^{-1}$) is unity, $R_{2-1/1-0}$ is the CO(1–0) to CO(2–1) integrated intensity ratio, $S_{\rm CO(2-1)}$ is the integrated CO(2–1) line flux in Jy km s^{-1}, and $D_{\rm L}$ is the luminosity distance to the source in Mpc. $R_{2-1/1-0} \simeq 0.8$ and 0.46 for NGC 3110 and NGC 232, respectively (see Section 4.3). In the range, the second value corresponds to a fixed correction factor to account for flux loss (see Section 4.1).

Table 4
Molecular Gas Concentrations (f_{con}) and Gas-to-dynamical Mass Ratios (f_{dyn})

Galaxy	R_{25} (kpc)	Σ_{mol}^{disk} ($M_\odot$ pc^{-2})	$\Sigma_{mol}^{1\,kpc}$ ($M_\odot$ pc^{-2})	f_{con}	$M_{mol}^{1\,kpc}$ (10^9 $M_\odot$)	$M_{dyn}^{1\,kpc}$ (10^9 $M_\odot$)	f_{dyn}
NGC 3110	19.6	8	306	38	0.9	14.9	0.06
NGC 232	12.2	21	455	22	1.1	39.1	0.03

5.2. Molecular Gas Excess and H I Deficiency

Given the ongoing interaction, the galaxies in these two systems are not in equilibrium and far from evolving secularly. NGC 3110 and NGC 232 have higher H_2-to-H I mass ratios (2.3 and 4.6, respectively) than the median value for isolated galaxies, ~0.4 (Lisenfeld et al. 2011), for similar morphological types. Note that we multiplied by a factor of 1.36 because the contribution of He was not originally included in the values of Lisenfeld et al. (2011). This large difference is due to the molecular gas content being larger and H I content smaller for a given stellar mass. The molecular gas masses of these two interacting galaxies, $\sim 2 \times 10^{10}\,M_\odot$ (Table 1), are well above the median for Sa–Sc isolated galaxies, $M_{mol} \simeq (0.6\text{–}1) \times 10^9\,M_\odot$ (Lisenfeld et al. 2011). Using the regression fit (ordinary least-squares fit with the *y*-axis as dependent variable, OLS(Y-X)) between log(M_{mol}) and log(L_B) for Sb–Sc isolated galaxies in (Lisenfeld et al. 2011, Table 7), we confirm that the molecular gas contents are in fact larger and not due to different galaxy sizes. The deficiency of molecular gas (or excess in this case) following the nomenclature in Lisenfeld et al. (2011), $DEF_{mol} = \log M_{mol,exp}$–$\log M_{mol,obs}$ (expected molecular gas mass, also corrected by the contribution of He, in log scale minus that observed), is –0.25 for NGC 3110 and –0.65 for NGC 232.

We also calculate the expected $M_{H\,I}$ following the regression fits between log($M_{H\,I}$) and log(L_B) (also OLS(Y-X)) for isolated galaxies (Jones et al. 2018, Table 6), and compare it to the observed $M_{H\,I}$ in Table 1. We follow similar conventions to obtain $M_{H\,I}$ and L_B as in Jones et al. (2018) (see also Verdes-Montenegro et al. 2005). The H I content in these two objects shows some level of deficiency, defined as $DEF_{H\,I} = \log M_{H\,I,exp}$—$\log M_{H\,I,obs}$ (expected atomic gas mass in log scale minus that observed), and is quantified to be 0.39 for NGC 3110 and 0.47 for NGC 232.

Therefore, the excess of molecular gas can be at least partially explained at the expense of H I. This is further discussed in Section 6.

5.3. Star Formation Activities

The global SFRs in both NGC 3110 and NGC 232 are of the order of $\sim 20\,M_\odot\,yr^{-1}$ (Table 1), larger than the typical values in noninteracting galaxies ($\sim 0.5\,M_\odot\,yr^{-1}$, Lisenfeld et al. 2011) or even in galaxies hosting a bar, where in general, large molecular gas concentrations can be found but the SFRs are typically of the order of $1\,M_\odot\,yr^{-1}$ within the inner 1 kpc (Sakamoto et al. 1999). The derived global Star Formation Efficiencies (SFE = SFR $[M_\odot\,yr^{-1}]/M_{mol}$ $[M_\odot]$) for both objects are $(1\text{–}2) \times 10^{-9}\,yr^{-1}$. This is closer to "normal" galaxies ($10^{-9}\,yr^{-1}$) than to the starburst sequence ($10^{-8}\,yr^{-1}$) (e.g., Daddi et al. 2010).

The Hα images are shown in Figure 2 for NGC 3110 (Hattori et al. 2004) and NGC 232 (Schmitt et al. 2006a). Note that their coordinate system presented some slight offsets of $<2''$ and their astrometry was calibrated by comparing the images with continuum maps with similar resolution and with accurate astrometry. After this correction, in general we see agreement between the CO(2–1) and Hα distributions in both objects.

In NGC 3110, the Hα emission of the circumnuclear region agrees well in extent and morphology with the CO(2–1) emission. The second brightest Hα component about $6''$ to the W of the nucleus is associated with another bright CO component as well. The third brightest Hα component is located in the southern arm at about $18''$ from the nucleus, but CO(2-1) emission is much dimmer there. The northern arm is substantially weaker in CO(2–1) emission than its southern counterpart, to the point that it is mostly undetected in our observations, even though H II regions are of comparable brightness in both arms and the distribution is more spread. The southern arm's CO(2–1) and Hα emissions overlap well, at least to our resolution element. However, there are regions that are bright in Hα emission but not detected in the CO(2–1) observations. These regions are north of the southern arm (~$6''$–$12''$ NE from the center), south of the northern arm (~6–$12''$ SW from the center), as well as some regions along both arms (and especially in the N arm).

The Hα emission morphology of NGC 232 is quite different. One of the most remarkable differences is that the spiral arms that are clearly seen in optical and NIR images do not present signs of SF, nor molecular gas to our sensitivity limit. The main component that is seen in CO(2–1) and Hα emissions is extended within a $10''$ (4.2 kpc) region and with a somewhat chaotic morphology if compared to NGC 3110. Hα emission also seems to be more diffuse and not as compact as that of the CO(2–1) emission. Hα emission and Paα (Tateuchi et al. 2015) are centrally peaked and seem to trace two nuclear spirals or shock regions, which likely drive gas to the nucleus. The Hα central and brightest component in the inner few arcsec corresponds to the location of the wings in the CO(2–1) profile. Also, there is some signature of molecular gas being more extended toward the SW from the center, but this is not clear in the Hα maps.

5.4. Spatially Resolved Star Formation Laws

We present the spatially resolved SF laws using the SMA CO(2–1) data as a tracer of the molecular gas surface densities (Σ_{mol}) and the Hα and *Spitzer* 24 μm maps for the SFR surface densities (Σ_{SFR}). Since Hα emission is affected by extinction, we estimate the amount of SF obscured by dust by using 24 μm data obtained with the MIPS instrument (Multiband Imaging Photometer for *Spitzer*, Rieke et al. 2004) on board the *Spitzer Space Telescope* (Werner et al. 2004). For the three maps we use a common astrometric grid and align them so that there are no artificial offsets. The Hα maps were compiled from Schmitt et al. (2006a) for NGC 232 and Hattori et al. (2004) for NGC 3110 (Section 5.3, see also Figure 2). We degraded the resolution of the Hα and CO(2–1) data to that of the *Spitzer*

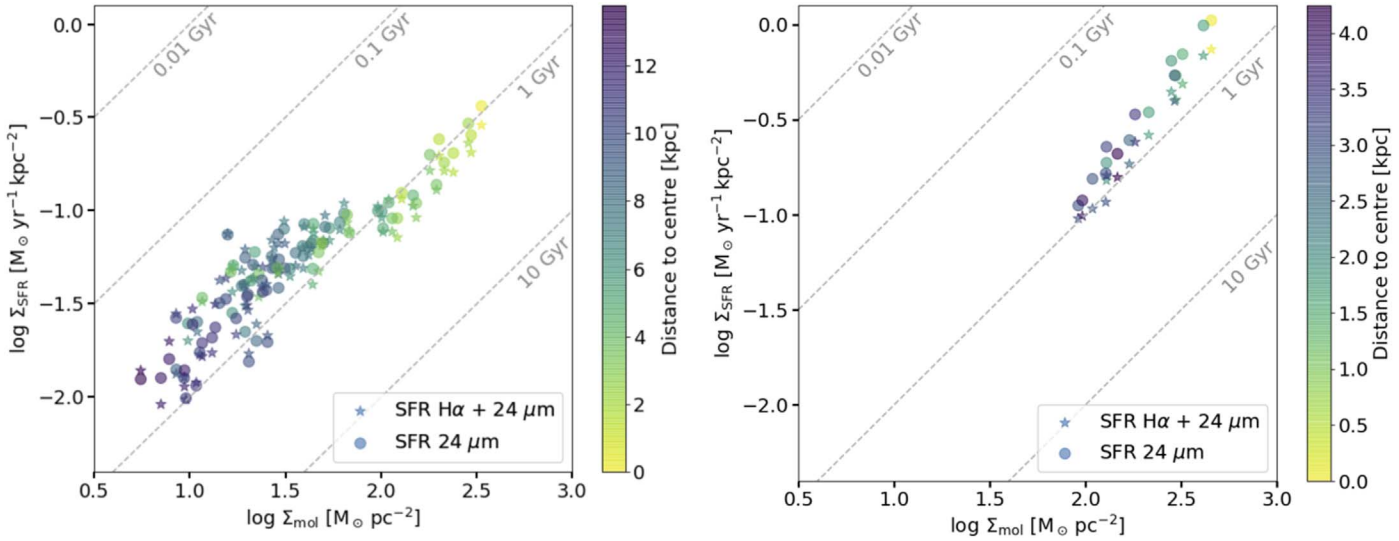

Figure 10. Star formation rate surface density ($\Sigma_{\rm SFR}$) estimated from Hα and 24 μm emission as a function of molecular gas surface density ($\Sigma_{\rm mol}$) from the CO(2–1) emission obtained for the two early stage merger galaxies NGC 3110 (left) and NGC 232 (right). Each data point corresponds to a 3.″1 pixel (resolution of the CO(2–1) data). Note that the resolution element of the 24 μm data is 6″. Dashed lines indicate constant depletion time lines expressed in Gyr. The color scale of the data points represents the distance from the center in kpc. Star symbols show data points with $\Sigma_{\rm SFR}$ estimated from Hα and 24 μm data, while circles show data points with $\Sigma_{\rm SFR}$ estimated from 24 μm only (see Section 5.4 for details).

24 μm data by convolving them with a circular Gaussian beam. The FWHM of the MIPS point-spread function (PSF) at 24 μm is 6″. The MIPS data are post-BCD (higher-level products) processed using the MIPS Data Analysis Tool (Gordon et al. 2005). We subtracted a background in both Hα and 24 μm maps, which were quite small.

The molecular surface densities, $\Sigma_{\rm mol}$, were obtained using the same convention as already indicated in Section 4.3 for $M_{\rm mol}$. The maps were corrected by the primary beam response. They are in units of $M_\odot\,{\rm pc}^{-2}$, include the contribution from Helium, and have been corrected by inclination. Our $\Sigma_{\rm mol}$ maps are sensitive to surface densities of $\Sigma_{\rm mol} \simeq 10\,M_\odot\,{\rm pc}^{-2}$.

Next, we constructed maps of the SFR surface densities, $\Sigma_{\rm SFR}$. We use the combination of Hα and 24 μm calibration convention as in Calzetti et al. (2010). We adopt the following prescription for the combination of the Hα and 24 μm maps to obtain the $\Sigma_{\rm SFR}$ (Calzetti et al. 2007, 2010): $\Sigma_{\rm SFR}$ $[M_\odot\,{\rm yr}^{-1}\,{\rm kpc}^{-2}] = 5.45 \times 10^{-42}$ ($S_{\rm H\alpha}$ [erg s^{-1} kpc^{-2}] + 0.031 S_{24} [erg s^{-1} kpc^{-2}]) where S_{24} and $S_{\rm H\alpha}$ denote the 24 μm and Hα luminosity surface densities, respectively. In this calibration of $\Sigma_{\rm SFR}$, Calzetti et al. (2007) adopts the default initial mass function in Starburst99 models (Leitherer et al. 1999), which is a Kroupa-type broken power law (Kroupa 2001). For comparison we also calculate $\Sigma_{\rm SFR}$ only using 24 μm data following $\Sigma_{\rm SFR}$ $[M_\odot\,{\rm yr}^{-1}\,{\rm kpc}^{-2}] = 2.75 \times 10^{-43}$ S_{24} [erg s^{-1} kpc^{-2}] (Wu et al. 2005; Calzetti et al. 2010). The global SFRs we obtain using Hα + 24 μm and only 24 μm are in agreement, 19.7 $M_\odot\,{\rm yr}^{-1}$ and 21.2 $M_\odot\,{\rm yr}^{-1}$ for NGC 3110, and 19.3 $M_\odot\,{\rm yr}^{-1}$ and 27.7 $M_\odot\,{\rm yr}^{-1}$ for NGC 232. The choice of either one of the SFR recipes does not have any remarkable impact on our main results. Also, these global SFR measurements agree with those obtained from the IR luminosities in Table 1.

We present in Figure 10 the $\Sigma_{\rm SFR}$ versus $\Sigma_{\rm mol}$ plots for both galaxies. The data points corresponding to the circumnuclear regions show $\Sigma_{\rm mol}$ up to $\sim 10^{2.5}\,M_\odot\,{\rm pc}^{-2}$, and depletion times of 1 Gyr for NGC 3110 and 0.8 Gyr NGC 232. In the plot for NGC 232 (Figure 10, right) we only show data points for the inner 12″ because the 24 μm map have artifacts caused by the PSF and the $\Sigma_{\rm SFR}$ values beyond could be uncertain.

In the case of NGC 3110, it is possible to compare the SF law for the circumnuclear and arm regions. The depletion times are on average 0.5 dex smaller at large radii than in the circumnuclear region. This may mean that the circumnuclear regions are not as efficient as the arms in transforming gas into stars. However, a smaller $X_{\rm CO}$ factor toward the center may contribute to the observed trend. Usually the $X_{\rm CO}$ factor is smaller in the nuclei of galaxies, especially in starbursts (Bolatto et al. 2013). A factor of 4 could explain this, i.e., from $X_{\rm CO} = 2 \times 10^{20}\,{\rm cm}^{-2}\,({\rm K\,km\,s}^{-1})^{-1}$, as we assumed, down to a $X_{\rm CO} = 0.5 \times 10^{20}\,{\rm cm}^{-2}\,({\rm K\,km\,s}^{-1})^{-1}$ in the circumnuclear regions, which might be a reasonable value in the central regions of a starburst galaxy. Assuming that $X_{\rm CO}$ factor does not vary, integrated fluxes about three times larger would be needed along the spiral arms to account for the 0.5 dex difference between the circumnuclear regions and spiral arms. It is unlikely that the data suffer from such a large amount of missing flux along the arms. Most of the missing flux should originate from a more extended component because the CO emission corresponding to the spiral arms (and in each channel) is expected to be relatively compact.

Figure 11 shows the $\Sigma_{\rm SFR}$ versus $\Sigma_{\rm mol}$ data points of NGC 3110 and NGC 232 over the plot of Figure 1 of Leroy et al. (2013) for all the data points in the HERACLES survey composed of 30 nearby disk galaxies. The adopted recipes to obtain $\Sigma_{\rm mol}$ and $\Sigma_{\rm SFR}$ are comparable. First, we can see that the data points in this study represent relatively high $\Sigma_{\rm mol}$ and $\Sigma_{\rm SFR}$ compared to 1 kpc regions in other "normal" galaxies. The depletion time of "normal" large disk galaxies as in Bigiel et al. (2008) and Leroy et al. (2013) is ~2 Gyr. Especially in the spiral arms of NGC 3110, the depletion times due to SFRs are on average ~0.5 dex larger than that in more quiescent galaxies. Regions at arms far away from the center lead to the "low metallicity dwarf galaxy region" in the plot of Leroy et al. (2013). Although SFEs are higher in the spiral arms, the

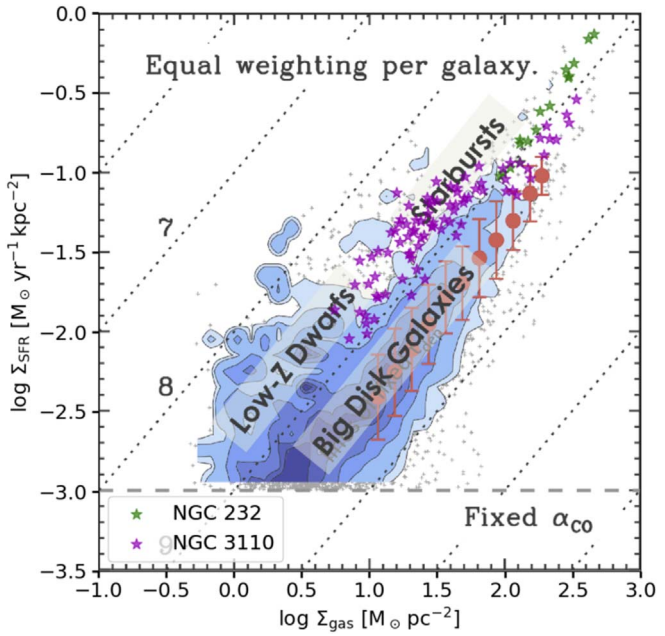

Figure 11. Star formation rate surface density (Σ_{SFR}) estimated from Hα and 24 μm emission as a function of molecular gas surface density (Σ_{mol}), extracted from Figure 1 of Leroy et al. (2013), together with the data points for NGC 3110 (magenta) and NGC 232 (green) in Figure 10 for comparison.

circumunclear regions seem to follow similar SFEs as in "normal" big disk galaxies if our assumed X_{CO} factor holds.

5.5. Distribution of Super Stellar Clusters in NGC 3110

Super star clusters (SSCs) are massive ($>10^5\,M_\odot$) and compact (a few parsec size) star clusters. SSCs and other complexes of clusters are usually found in merging systems close to dense molecular clouds (e.g., Whitmore & Schweizer 1995; Whitmore et al. 2007; Espada et al. 2012; Herrera & Boulanger 2017), and starburst dwarf galaxies (e.g., Miura et al. 2015, 2018; Turner et al. 2015). The properties of SSCs seem to be different depending on the stage of the merger: SSCs in post-mergers are usually more luminous, larger and redder than in interacting systems in the early stages (Miralles-Caballero et al. 2011).

NGC 3110 was observed with VLT/NACO as part of the SUNBIRD (SUperNovae and starBursts in the InfraReD) survey (Randriamanakoto & Väisänen 2017). Figure 12 (left panel) shows the location of the Ks-band candidate SSCs as compared with our CO map. The resolution of the Ks-band map is $\sim$0.″1. It is remarkable that at least $\sim$350 SSCs were found in this object and they are located mostly along the spiral arms and its circumnuclear component (Randriamanakoto 2015). Although SSCs are commonly seen in (intermediate/late stage) mergers (e.g., Whitmore & Schweizer 1995; Whitmore et al. 2007), this proves that even in an initial phase of the merger, and even when the interacting galaxy mass ratio is so large, a substantial population of SSCs can be formed. We see that the distribution of SSCs in the northern and southern arms seem more symmetric to each other than in CO emission. Even though the number of SSCs formed along the two arms is similar, the molecular gas surface densities are at least a factor of five smaller or even mostly depleted in the northern arm.

Figure 12 (right panel) shows the SSC number surface density (to the resolution of the CO(2–1) map) versus Σ_{gas} plot. There is a correlation in the sense that regions with higher gas surface densities host a larger number of SSCs. The Spearman's correlation coefficient (log scale) is $\rho = 0.8$.

Furthermore, the luminosity functions of SSCs separating the circumnuclear regions and outer regions (arms) have been studied by Randriamanakoto (2015), and it has been found that in the circumnuclear regions the luminosity function is flatter than in the external parts ($\alpha = 1.96 \pm 0.08$ versus $\alpha = 2.35 \pm 0.09$). This may mean that the formation of the most massive SSCs depends on their environment and occur preferentially in regions with high molecular gas surface densities (and SFR surface densities). The difference in the LF power-law slopes could also be partly caused by blending effects and the difficulty of detecting faint NIR clusters in the circumnuclear regions. However, the blending effect is unlikely to be important for targets less distant than 100 Mpc (Randriamanakoto et al. 2013).

6. Discussion

We discuss the properties of the molecular gas derived from our CO(2–1) observations of NGC 3110 and NGC 232, as well as the resulting star formation activities, in the context of published numerical simulations of interacting systems and other observational work. We also present our own numerical simulations trying to reproduce the properties of the NGC 3110 system.

6.1. Comparison of Distribution and SF Activities with Numerical Simulations

It is known from numerical simulations that early stage merger interactions may generate asymmetric two-armed spirals, warps, bars, and tidal tails that extend well beyond the main body of the galaxy (see Section 1). A number of numerical studies have explored the parameter space of minor encounter/merger scenarios (e.g., Struck et al. 2011; Oh et al. 2015; Pettitt et al. 2015), including how changes in mass and impact parameters affect the stellar and gaseous components for a galaxy interacting with a companion that is at least an order of magnitude less massive than the host, which matches reasonably well with the situation of NGC 3110. With these kinds of low mass companions an $m = 2$ response (i.e., spiral arms) is easily produced (within reasonable approach distances and velocity differences). As in the simulations, our NGC 3110 maps show the two-armed molecular component, which dominates outside a few kpc. Higher mass companions are seen to disrupt the disks to the extent that spirals are not as clear, resulting in rings and less regular features, possibly in agreement with the less prominent spiral arms in NGC 232. It may also be possible that the interaction in NGC 232 is simply not oriented in the correct manner (i.e., against rotation), which has been seen to produce only a minor morphological response (D'Onghia et al. 2010; Łokas 2018). Stronger tidal forces are, however, more efficient at driving spiral features into the inner disk (<2 kpc) than weaker interactions. A gaseous disk is detected in NGC 232 at inner radii, with little CO or Hα emission present in the form of spiral arms, which might be in agreement with a strong interaction scenario. Also, these simulations showed that higher mass companion galaxies may reduce the effective size of the main galaxy by a few kpc compared to interactions with lighter companions, causing rapid infall and stripping of the outer material, which both aid in reducing disk scale lengths.

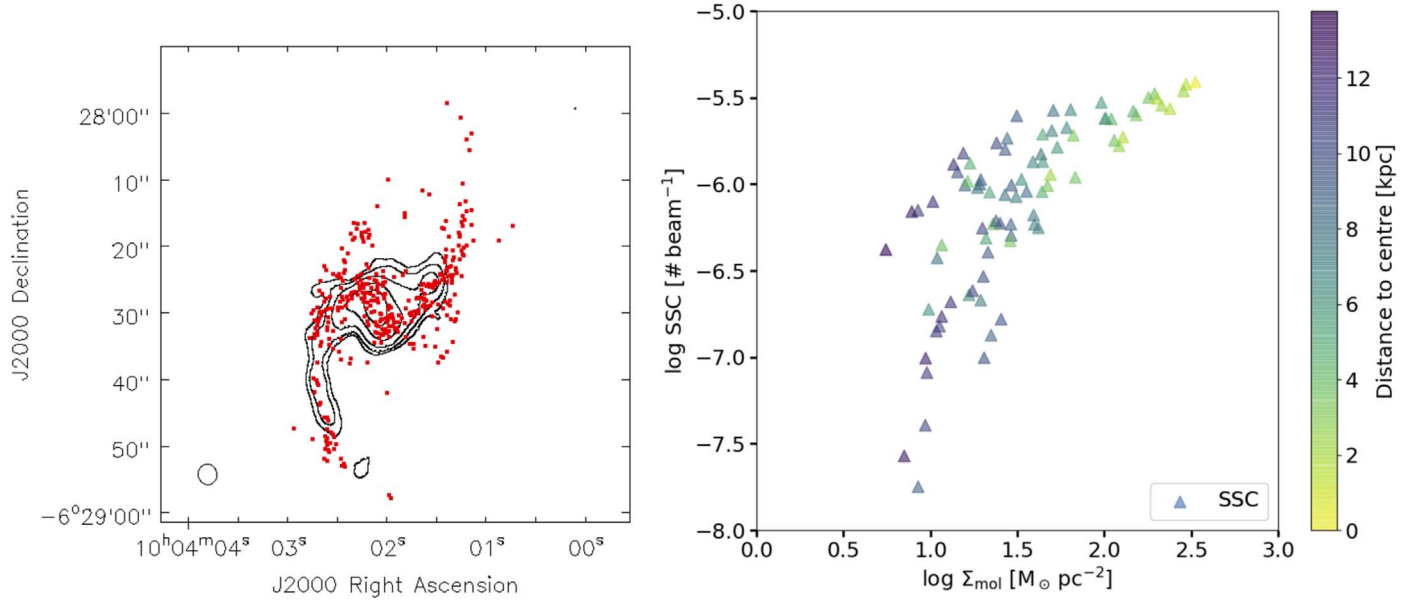

Figure 12. Left: distribution of identified SSCs based on a Ks-band image of NGC 3110 obtained with VLT/NACO, with the CO(2–1) contours on top as in Figure 6. Right: pixel-to-pixel correlation between SSC number surface density and molecular gas surface density ($\Sigma_{\rm mol}$). The color scale of the data points represents the distance from the center in kpc.

Preliminary numerical simulations including self gravity, cooling, star formation and feedback of a tidally induced two-armed galaxy with similar properties as NGC 3110 are briefly presented here, carried out with the GASOLINE2 SPH code (Wadsley et al. 2017). The evolution of the merger in different epochs around the first approach is shown in Figure 13. For more details, please refer to Pettitt et al. (2017), for a similar experiment of a fly-by interaction between a disk galaxy and smaller companion, although not optimized to reproduce the properties of this system. The primary galaxy has a mass model and rotation curve constrained to that observed for NGC 3110, with velocity dispersions in the stars set to slow the bar formation and create a multi-armed spiral when evolved in isolation. We assume a total mass ratio of 14:1, and a similar velocity difference and separation as observed in the NGC 3110 system. The tidal forces induce a two-armed structure in the simulation that matches the distribution seen in our maps of NGC 3110 reasonably well at about 150 Myr after the closest approach (see Figure 13), with clear asymmetries seen between the two spiral arms and a kink in orientation at the end of the southern arm.

However, the central star-forming activities found in the observations are not as well reproduced by numerical simulations. The galaxy mass ratio has been identified in other numerical simulations as a main parameter characterizing the resulting merger driven starburst. But the induced SF for mass ratios larger than 10:1 is seen to be almost negligible in other works (e.g., Cox et al. 2008). This is in contrast with our observational results, where the total SFR (SFRs $\sim 20\,M_{\odot}\,{\rm yr}^{-1}$) is as high as that expected in other numerical simulations for some similarly sized galaxy interactions. The starburst efficiency depends on the structure of the primary galaxy, and in particular, the lack of a massive stellar bulge will make the disk unstable and will enhance merger driven SF even for large mass ratio mergers (Cox et al. 2008). The SFRs in the simulations of Pettitt et al. (2017) (Figure 8) for a system of mass ratio 10:1 are also low, probably as a result of the inclusion of a massive bulge (and halo). Additionally, the gas only constitutes 10% of the baryonic component in the simulation, which is substantially lower than both our target galaxies, which would also result in a lower SFR in comparison. In these simulations the peak is $6\,M_{\odot}\,{\rm yr}^{-1}$ and average $2\,M_{\odot}\,{\rm yr}^{-1}$. Other simulations in the literature of stronger bound interactions (clearly resulting in mergers) can reproduce SFRs of up to $100\,M_{\odot}\,{\rm yr}^{-1}$ (Hopkins et al. 2013; Renaud et al. 2015), though result in clearly disrupted disks and clear gas bridges between the interacting pairs. The SFR history of our simulations is presented in Figure 14. Although there is a peak of about $25\,M_{\odot}\,{\rm yr}^{-1}$ at about 620 Myr since tidal interaction started, that corresponds to ~70 Myr after our best morphological match. At any rate, the current status of NGC 3110 may represent one of the highest SFR episodes as a result of the interaction with the minor companion (before coalescence), likely just after closest approach. The specific case of the NGC 3110 interaction and the resulting morphology in dense gas, clusters, and localized SF will be the subject of a future numerical study with higher spatial resolution than presented here.

6.2. Conversion from H I into Molecular Gas and Gas Inflow

In the relatively early stages of the interaction of the NGC 3110 and NGC 232 systems we found an excess of molecular gas that can be at least partially explained as a result of the conversion of H I (Section 5.2). An excess of molecular gas is also seen in the early evolutionary phase of more extreme systems such as Hickson Compact Groups, HCGs, which might also be linked to H I deficiencies (Martinez-Badenes et al. 2012). These results are in agreement with simulations, where an increase in the molecular to H I fraction even in the early stages of a merger can be seen, with one the largest events occurring immediately after the first close approach (Iono et al. 2004). Using single-dish observations, Yamashita et al. (2017)

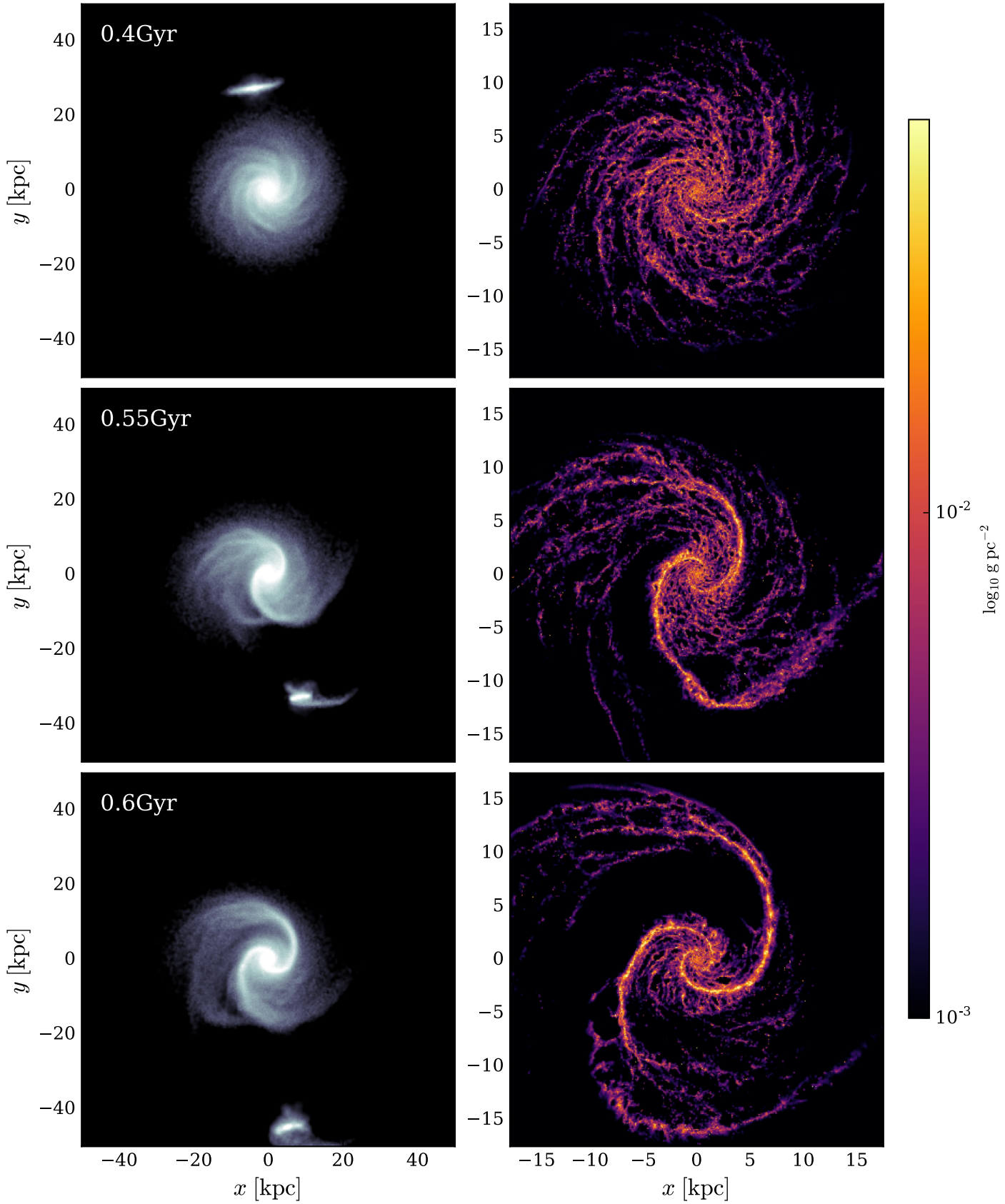

Figure 13. Numerical simulations reproducing the morphological properties of the NGC 3110 system. The plots show, from top to bottom, different epochs of the early stage merger, at 0.40, 0.55 (best match), and 0.60 Gyr. Left panels show the stellar component while right panels show the gaseous component. Note the different spatial scales between left and right.

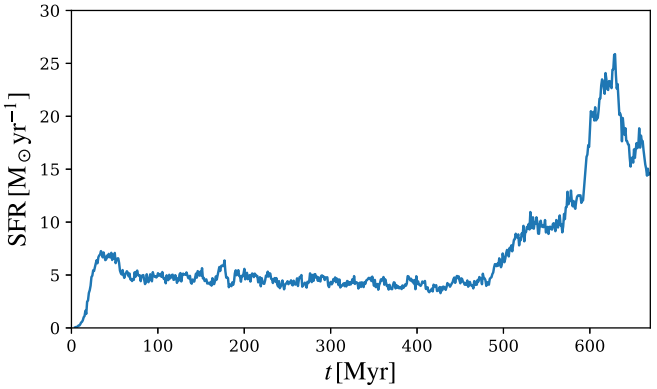

Figure 14. SFR history obtained from our numerical simulations of NGC 3110 during the first 700 Myr since tidal interaction started. The closest approach occurs at 460 Myr, and the current epoch based on a morphological match is at about 550 Myr.

found that the molecular gas mass in the central several kpc seems to be constant from early stage to late stage mergers, and they inferred that molecular gas inflows replenish the consumed gas by SF. The excess of molecular gas in the two galaxies studied here can probably be explained partly by molecular gas inflow from the outer regions, but also by the conversion from H I into molecular gas. Kaneko et al. (2017) found that there is a high global molecular gas fraction in a sample of four mid-stage mergers and they suggest an efficient transition from atomic to molecular gas due to external pressure as a result of the interaction. The molecular hydrogen gas mass to total (atomic plus molecular hydrogen) gas mass averaged over their sample of galaxies is 0.71 ± 0.15, in agreement with the 0.66 for NGC 3110 and 0.78 for NGC 232 we obtain following their convention. Once H I is consumed or lost, then one would naturally find that the molecular content decreases with decreasing projected separation between the nuclei of the merging galaxies, as SF consumes the available gas and the merger stage advances (Gao & Solomon 1999).

In NGC 3110, the molecular gas concentration might be as large as that produced by a bar (Section 4.4). We argue that interactions with a minor companion can be a mechanism to build large gas central concentrations in galaxies, triggering starbursts and feeding AGNs, without the need of a bar. One of our results is that there is a net positive inflow rate to the circumnuclear regions. The additional centrally concentrated mass due to the interaction can be estimated to be a few percent of the total molecular gas mass, by comparing the observed surface density of the interacting system with the average of non-barred galaxies. In the case of NGC 3110, the extra mass that is expected to have been deposited into the inner 500 pc is $\sim 5 \times 10^8\, M_\odot$ (as estimated from Section 4.4) in about 150 Myr (from the best morphological match with the numerical simulations, Section 6.1), and therefore the molecular gas inflow rate is around $3\, M_\odot\, \mathrm{yr}^{-1}$. The molecular gas will accumulate in the inner region because the observed SFR in that area is two times smaller than the inflow rate.

There is a peak in the SF history of mergers occurring mostly in centrally concentrated starbursts triggered during coalescence, when shocks drive large quantities of gas and dust into the nuclear regions (e.g., Lonsdale et al. 2006). Gas can also be channeled into the nuclear regions of the progenitors due to the tidal forces during the first close approach, and this should be a noteworthy epoch in the evolution of these systems. We find in

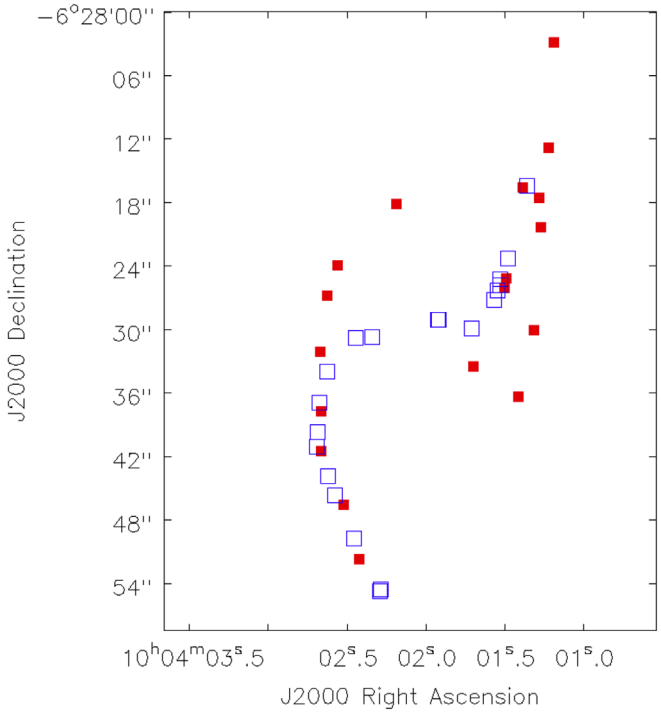

Figure 15. Data points representing the location of some of the main molecular clumps (blue open squares) and H II regions (red filled squares) along the two spiral arms obtained from two-dimensional Gaussian fits on the images shown in Figure 2 (left). See Section 6.3 for details.

the two objects under study that starbursts with gas surface densities of $\gtrsim 10^{2.5}\, M_\odot$ can be found that, although small by an order of magnitude compared to those in ULIRGs, are considerably larger than in an average noninteracting galaxy. We also note that soon after the first approach, spiral arms and other filaments are formed, where gas is efficiently compressed and high SFRs produced (see Figure 13). This is in agreement with high-resolution numerical simulations in Teyssier et al. (2010), who argue that one of the dominant processes in the increase of SFR is actually gas fragmentation into massive and dense clouds along filaments that can be far away from the center and where SF occurs efficiently. Moreover, from the derived SF history of the numerical simulation of a system like Antennae (Figure 2, Teyssier et al. 2010), we can see that although during coalescence there are extreme values of SFR (with a peak in SFR one order of magnitude larger than during the approaching phase), the total amount of SF during that shorter period of about 100 Myr, is comparable to that in the period between the first and second pericenters (~200 Myr). To our knowledge, simulations of minor mergers (whose merging process lasts for a longer period of time) such as the case of NGC 3110 do exist in the literature but do not in general study the SF history, and it would be worth further investigation.

6.3. Distribution of Molecular Gas, H II Regions, and Formation of SSCs in NGC 3110

In NGC 3110, Hα and the molecular gas emissions are well correlated spatially. In the CO interferometric observations we estimate that the position accuracy is of the order of $\theta/(2 \times \mathrm{S/N})$ (Reid et al. 1988), where θ is the beam size and S/N is the signal-to-noise ratio, so for regions detected with $\mathrm{S/N} \sim 5$ the accuracy is roughly 1/10 of the beam size. If we add other sources of

uncertainties such as phase calibration, we estimate that the accuracy is no better than 1/5, or 0.″6 (210 pc). In Figure 15 we present a comparison of the locations of the main molecular clumps and H II regions along the two spiral arms. The identification of the molecular clumps was performed on the CO(2–1) channel map. For each channel we selected the main clumps above a threshold of 0.09 Jy beam^{-1} along the arms (excluding the circumnuclear regions) and we fitted Gaussian curves around the peaks to obtain their central positions. For the Hα data points, we used a threshold of 6×10^{-16} erg s^{-1} cm^{-2} in the Hα map and obtained the central positions in the same manner. We note that although the identification of molecular clumps and H II regions is not complete, it serves to investigate a possible offset between both components.

The lack of an offset in the southern arm is in agreement with simulations that suggest that shocks in dynamic arms show little to no spatial offsets between stellar and gas arms (Wada et al. 2011; Baba et al. 2015). Simulations of tidal arms give a more mixed picture, with some simulations showing little evidence of offsets (e.g., Dobbs et al. 2010; Struck et al. 2011), and others showing clear and often very large offsets (up to half a kpc) that are not uniform in time or location in the disk (Pettitt et al. 2016, 2017). It is important to note however that M51, a clearly interacting system, displays some of the clearest evidence for offsets between arm tracers (e.g., Egusa et al. 2017). It may be that offsets in the southern arm have simply not manifested yet, or that they are not detectable with the current spatial resolution. We cannot discount that an offset exists in the northern arm as large portions of it remain undetected in CO emission.

Hundreds of SSCs were found along the filamentary structures of NGC 3110 (Section 5.5). SSCs have been seen to form in mergers, even at several kpc from their center, as in Antennae galaxies (Whitmore & Schweizer 1995). However, our comparison proves that in an initial phase of the merger, and even when the interacting galaxy mass ratio is large, a substantial population of SSCs can be formed. The distribution of SSCs in the northern and southern arms seem to be more symmetric to each other than in the CO emission, and match well with the H II regions. Molecular gas surface densities are at least a factor of five smaller in the northern arm. There is also a region almost at the end of the southern arm where there is a higher density of SSCs, bright Hα, but quite weak CO emission. Although in general the molecular clumps and H II regions along the southern arm are well co-located, we find that there are regions that are weak in CO and are clearly detected in Hα emission, specifically the northern side of the opposite arm, which is less confined than the one in the south, as well as about 6″–12″ to the NE and SW from the nucleus. These could be explained by molecular gas being consumed by SF, and then ionized and destroyed by the radiation and winds of the resulting SSCs. The lifetime of the molecular arms can be quite reduced due to this, in addition to the gas flows to the center. If the arms are not replenished by external gas, the lifetime will be of the order of 0.5 Gyr based on the SFEs we find there.

7. Summary and Conclusions

We presented maps of the bulk of molecular gas of the spiral galaxies NGC 3110 and NGC 232 as traced by the CO(2–1) line using the SMA, both in an early stage phase merger and classified as LIRGs. While NGC 3110 is interacting with a minor companion whose stellar mass is smaller by a factor of 14 at a distance of 38 kpc and velocity difference of $\Delta V = 235$ km s^{-1}, NGC 232 is interacting with a similarly sized object at a distance of 50 kpc and $\Delta V = 120$ km s^{-1} (projected along the line of sight). The angular resolution achieved in our CO(2–1) observations with SMA is ∼3.″2, or 1.1 and 1.3 kpc, respectively. Our results illustrate the properties of molecular gas and star formation in the early stages of an interaction well before coalescence. Our main findings are summarized as follows:

1. The tidal interactions are likely the primary cause to induce the formation of spiral arms and starburst events in the main galaxies. The molecular gas properties of the two objects are remarkably different. While NGC 3110 presents molecular gas along the (stellar) spiral arms, no detection is found to our sensitivity limit along the spiral arms of NGC 232. The distribution and kinematics of the molecular gas and Hα emission of NGC 232 are found to be more centrally concentrated and chaotic than in the case of NGC 3110. These different properties are likely due to the larger tidal forces exerted on NGC 232.
2. There is an excess of molecular gas mass ($\mathrm{DEF_{mol}} = -0.3$ to -0.6) compared with noninteracting galaxies with similar stellar luminosities and morphological types. At the same time we find H I deficiency of about $\mathrm{DEF_{H\,I}} = 0.4$–$0.5$ in the two objects, which leads us to argue that the molecular gas excess might be partly due to the conversion of atomic gas content into molecular gas.
3. The molecular gas concentration, calculated as the ratio of surface densities corresponding to the circumnuclear region and the whole optical disk, is at the high end of non-strongly interacting and non-barred objects, and comparable to the low end of barred galaxies. This suggests that in the early stages of the interaction, the main responsible mechanism for the gas to be driven to galactic centers is the interaction itself, at least in the case of NGC 3110, and its amplitude can be as important as in a barred system. By comparing its morphology to numerical simulations with similar parameters and the observed concentrations of non-barred noninteracting galaxies from the literature, we estimated that the gas flow rate is $\sim 3\,M_\odot$ yr^{-1} in the case of NGC 3110. With this gas flow rate the current SFR will be sustained and may probably even increase.
4. The molecular gas and SFR surface densities in the circumnuclear regions of these two objects ($\Sigma_{\mathrm{mol}} \gtrsim 10^{2.5}\,M_\odot$ pc^{-2}, $\Sigma_{\mathrm{SFR}} \simeq 10^{-0.5}\,M_\odot$ pc^{-2}, for 1 kpc) are one order of magnitude higher than in noninteracting objects, but smaller than in ULIRGs also by an order of magnitude. In terms of SFE all the molecular clouds are in an intermediate position between the disk galaxies and the starbursts. In NGC 3110 the gas depletion time is 0.5 dex smaller in the spiral arms compared to the circumnuclear region. A possible explanation is that SFE is higher along the spiral arms, although we note that a different X_{CO} conversion factor and missing flux could affect this conclusion.
5. Numerical simulations agree well with our observations in terms of morphological appearance, and in particular for the case of interactions with small companions such as NGC 3110. The distribution of the two arms found in the light companion simulations matches reasonably well with the distribution seen in our maps of NGC 3110 at ∼150 Myr after the closest approach. The current status

of NGC 3110 may represent one of the highest SFR episodes as a result of the interaction with the minor companion before coalescence. We also note differences with the numerical simulations, in the sense that the resulting SFR and molecular gas densities are not as large or at the same epoch as in our observational results in the minor companion case. The more chaotic distribution in NGC 232 and the weaker gaseous spiral arms (if any) are in general well reproduced by simulations of more massive companions.

6. A large population of >350 super stellar clusters (SSCs) were found in NGC 3110 (to our knowledge no such observations exist for NGC 232 yet). They are mostly confined within the circumnuclear regions and along the spiral arms. There is a correlation between molecular gas and the existence of SSCs, in the sense that regions with higher molecular gas surface densities host a larger number of SSCs.
7. In general, we find that molecular clumps, H II regions, and SSCs are well co-located. We do not find large offsets (to about 200 pc) between the stellar, ionized, and molecular components along most of the southern arm. However, we note that there are some deviations. Some regions that present weak or no CO emission are clearly detected in Hα emission, and have a large population of SSCs. This is most obvious in the northern side of the northern arm, which is less confined than the one in the S, as well as about 6″–12″ to the NE and SW from the nucleus, and the far end of the southern arm. These could be explained by differences in the gas densities on the different sides of the galaxy as seen in simulations, radial gas inflows, and/or molecular gas being consumed by SF, and then ionized and destroyed by the radiation and winds of the resulting star formation, and in particular SSCs.

We thank the referee for the careful reading and valuable suggestions that helped to improve this paper substantially. This research made use of the NASA/IPAC Extragalactic Database (NED), which is operated by the Jet Propulsion Laboratory, California Institute of Technology, under contract with the National Aeronautics and Space Administration. We acknowledge the usage of the HyperLeda database (http://leda.univ-lyon1.fr). We thank Dr. T. Hattori and Dr. H. Schmitt for kindly providing Hα maps used in this paper to derive the SF laws. D.E. was supported by a Marie Curie International Fellowship within the Sixth European Community Framework Programme (MOIF-CT-2006-40298). S.V. acknowledges support by the research projects AYA2014-53506-P and AYA2017-84897-P from the Spanish Ministerio de Economia y Competitividad, from the European Regional Development Funds (FEDER) and the Junta de Andalucia (Spain) grants FQM108. T.S. acknowledges funding from the European Research Council (ERC) under the European Union's Horizon 2020 research and innovation programme (grant agreement No. 694343). L.V.M. acknowledges support from the grant AYA2015-65973-C3-1-R (MINECO/FEDER, UE). S. Matsushita is supported by the Ministry of Science and Technology (MOST) of Taiwan, MOST 106-2112-M-001-011 and 107-2119-M-001-020. M.A.F. is grateful for financial support from the CONICYT Astronomy Program CAS-CONICYT project No. CAS17002, sponsored by the Chinese Academy of Sciences (CAS), through a grant to the CAS South America Center for Astronomy (CASSACA) in Santiago, Chile. This research made use of Astropy, a community-developed core Python (http://www.python.org) package for Astronomy (Astropy Collaboration et al. 2013; The Astropy Collaboration et al. 2018); ipython (Perez & Granger 2007); matplotlib (Hunter 2007); APLpy, an open-source plotting package for Python (Robitaille & Bressert 2012) and NumPy (Van Der Walt et al. 2011). We utilized the pynbody python package (Pontzen et al. 2013) for post-processing and analyzing of the tipsy files created by gasoline2. Special thanks to the authors of gasoline2 (Wadsley et al. 2017) for providing the numerical code used to perform the simulations. Part of this work was achieved using the grant of Visiting Scholars Program supported by the Research Coordination Committee, National Astronomical Observatory of Japan (NAOJ), National Institutes of Natural Sciences (NINS). D.E. was supported by JSPS KAKENHI grant No. JP 17K14254.

Facilities: SMA, *Spitzer*.

ORCID iDs

Daniel Espada https://orcid.org/0000-0002-8726-7685
Zara Randriamanakoto https://orcid.org/0000-0003-2666-4158
Pei-Ying Hsieh https://orcid.org/0000-0001-9155-3978
Toshiki Saito https://orcid.org/0000-0002-2501-9328
Rie E. Miura https://orcid.org/0000-0001-8187-7856
Lourdes Verdes-Montenegro https://orcid.org/0000-0003-0156-6180
Ryohei Kawabe https://orcid.org/0000-0002-8049-7525
Daisuke Iono https://orcid.org/0000-0002-2364-0823

References

Albrecht, M., Krügel, E., & Chini, R. 2007, A&A, 462, 575
Argudo-Fernández, M., Verley, S., Bergond, G., et al. 2013, A&A, 560, A9
Argudo-Fernández, M., Verley, S., Bergond, G., et al. 2014, A&A, 564, A94
Argudo-Fernández, M., Verley, S., Bergond, G., et al. 2015, A&A, 578, A110
Armus, L., Mazzarella, J. M., Evans, A. S., et al. 2009, PASP, 121, 559
Astropy Collaboration, Robitaille, T. P., Tollerud, E. J., et al. 2013, A&A, 558, A33
Baba, J., Morokuma-Matsui, K., & Egusa, F. 2015, PASJ, 67, L4
Barnes, D. G., Staveley-Smith, L., de Blok, W. J. G., et al. 2001, MNRAS, 322, 486
Barnes, J. E., & Hernquist, L. 1992, ARA&A, 30, 705
Barnes, J. E., & Hernquist, L. 1996, ApJ, 471, 115
Bigiel, F., Leroy, A., Walter, F., et al. 2008, AJ, 136, 2846
Bolatto, A. D., Wolfire, M., & Leroy, A. K. 2013, ARA&A, 51, 207
Bridge, C. R., Carlberg, R. G., & Sullivan, M. 2010, ApJ, 709, 1067
Bryant, P. M., & Scoville, N. Z. 1999, AJ, 117, 2632
Bushouse, H. A. 1987, ApJ, 320, 49
Calzetti, D., Kennicutt, R. C., Engelbracht, C. W., et al. 2007, ApJ, 666, 870
Calzetti, D., Wu, S.-Y., Hong, S., et al. 2010, ApJ, 714, 1256
Chini, R., Kruegel, E., & Lemke, R. 1996, A&AS, 118, 47
Colina, L., Piqueras López, J., Arribas, S., et al. 2015, A&A, 578, A48
Corbett, E. A., Kewley, L., Appleton, P. N., et al. 2003, ApJ, 583, 670
Corbett, E. A., Norris, R. P., Heisler, C. A., et al. 2002, ApJ, 564, 650
Cox, A. N. 2000, Allen's Astrophysical Quantities (New York: Springer-Verlag)
Cox, T. J., Jonsson, P., Somerville, R. S., Primack, J. R., & Dekel, A. 2008, MNRAS, 384, 386
Coziol, R., Iovino, A., & de Carvalho, R. R. 2000, AJ, 120, 47
Daddi, E., Elbaz, D., Walter, F., et al. 2010, ApJL, 714, L118
Dame, T. M., Hartmann, D., & Thaddeus, P. 2001, ApJ, 547, 792
de Vaucouleurs, G., de Vaucouleurs, A., Corwin, H. G., Jr., et al. 1991, Third Reference Catalogue of Bright Galaxies, Vol. I, II, III (New York: Springer-Verlag)
Dobbs, C. L., Theis, C., Pringle, J. E., & Bate, M. R. 2010, MNRAS, 403, 625
D'Onghia, E., Vogelsberger, M., Faucher-Giguere, C.-A., & Hernquist, L. 2010, ApJ, 725, 353
Dopita, M. A., Pereira, M., Kewley, L. J., & Capaccioli, M. 2002, ApJS, 143, 47

Downes, D., & Solomon, P. M. 1998, ApJ, 507, 615
Dubinski, J., & Chakrabarty, D. 2009, ApJ, 703, 2068
Egusa, F., Mentuch Cooper, E., Koda, J., & Baba, J. 2017, MNRAS, 465, 460
Ellison, S. L., Patton, D. R., Simard, L., & McConnachie, A. W. 2008, AJ, 135, 1877
Espada, D., Komugi, S., Muller, E., et al. 2012, ApJL, 760, L25
Espada, D., Martin, S., Hsieh, P.-Y., et al. 2010, in Galaxies and their Masks, ed. D. L. Block, K. C. Freeman, & I. Puerari (New York: Springer-Verlag), 97
Espada, D., Verdes-Montenegro, L., Huchtmeier, W. K., et al. 2011, A&A, 532, A117
Gao, Y., & Solomon, P. M. 1999, ApJL, 512, L99
Gordon, K. D., Rieke, G. H., Engelbracht, C. W., et al. 2005, PASP, 117, 503
Greve, T. R., Papadopoulos, P. P., Gao, Y., & Radford, S. J. E. 2009, ApJ, 692, 1432
Hattori, T., Yoshida, M., Ohtani, H., et al. 2004, AJ, 127, 736
Herrera, C. N., & Boulanger, F. 2017, A&A, 600, A139
Ho, P. T. P., Moran, J. M., & Lo, K. Y. 2004, ApJL, 616, L1
Hopkins, P. F., Cox, T. J., Hernquist, L., et al. 2013, MNRAS, 430, 1901
Hunter, J. D. 2007, CSE, 9, 90
Imanishi, M., & Nakanishi, K. 2013, AJ, 146, 47
Imanishi, M., Nakanishi, K., Tamura, Y., & Peng, C.-H. 2009, AJ, 137, 3581
Iono, D., Saito, T., Yun, M. S., et al. 2013, PASJ, 65, L7
Iono, D., Wilson, C. D., Yun, M. S., et al. 2009, ApJ, 695, 1537
Iono, D., Yun, M. S., & Ho, P. T. P. 2005, ApJS, 158, 1
Iono, D., Yun, M. S., & Mihos, J. C. 2004, ApJ, 616, 199
Iovino, A. 2002, AJ, 124, 2471
Jones, M. G., Espada, D., Verdes-Montenegro, L., et al. 2018, A&A, 609, A17
Kaneko, H., Kuno, N., Iono, D., et al. 2017, PASJ, 69, 66
Kennicutt, R. C., Jr. 1998a, ARA&A, 36, 189
Kennicutt, R. C., Jr. 1998b, ApJ, 498, 541
Kim, J. H., Peirani, S., Kim, S., et al. 2014, ApJ, 789, 90
Kroupa, P. 2001, MNRAS, 322, 231
Lang, M., Holley-Bockelmann, K., & Sinha, M. 2014, ApJL, 790, L33
Larson, K. L., Sanders, D. B., Barnes, J. E., et al. 2016, ApJ, 825, 128
Leitherer, C., Schaerer, D., Goldader, J. D., et al. 1999, ApJS, 123, 3
Leroy, A. K., Walter, F., Sandstrom, K., et al. 2013, AJ, 146, 19
Lisenfeld, U., Espada, D., Verdes-Montenegro, L., et al. 2011, A&A, 534, A102
Łokas, E. L. 2018, ApJ, 857, 6
Lonsdale, C. J., Farrah, D., & Smith, H. E. 2006, in Ultraluminous Infrared Galaxies, ed. J. W. Mason, 285
López-Cobá, C., Sánchez, S. F., Cruz-González, I., et al. 2017, ApJL, 850, L17
López-Sanjuan, C., Cenarro, A. J., Varela, J., et al. 2015, A&A, 576, A53
Makarov, D., Prugniel, P., Terekhova, N., Courtois, H., & Vauglin, I. 2014, A&A, 570, A13
Malkan, M. A., Gorjian, V., & Tam, R. 1998, ApJS, 117, 25
Martin, J. M., Bottinelli, L., Gouguenheim, L., & Dennefeld, M. 1991, A&A, 245, 393
Martín, S., George, M. R., Wilner, D. J., & Espada, D. 2010, AJ, 139, 2241
Martinez-Badenes, V., Lisenfeld, U., Espada, D., et al. 2012, A&A, 540, A96
McMullin, J. P., Waters, B., Schiebel, D., Young, W., & Golap, K. 2007, in ASP Conf. Ser. 376, Astronomical Data Analysis Software and Systems XVI, ed. R. A. Shaw, F. Hill, & D. J. Bell (San Francisco, CA: ASP), 127
Mihos, J. C., & Hernquist, L. 1996, ApJ, 464, 641
Mihos, J. C., Richstone, D. O., & Bothun, G. D. 1992, ApJ, 400, 153
Mirabel, I. F., Booth, R. S., Johansson, L. E. B., Garay, G., & Sanders, D. B. 1990, A&A, 236, 327
Miralles-Caballero, D., Colina, L., Arribas, S., & Duc, P.-A. 2011, AJ, 142, 79
Miura, R. E., Espada, D., Hirota, A., et al. 2018, arXiv:1808.10089
Miura, R. E., Espada, D., Sugai, H., Nakanishi, K., & Hirota, A. 2015, PASJ, 67, L1
Moore, B., Katz, N., Lake, G., Dressler, A., & Oemler, A. 1996, Natur, 379, 613
Oh, S. H., Kim, W.-T., & Lee, H. M. 2015, ApJ, 807, 73
Papadopoulos, P. P., van der Werf, P., Xilouris, E., Isaak, K. G., & Gao, Y. 2012, ApJ, 751, 10
Patton, D. R., Torrey, P., Ellison, S. L., Mendel, J. T., & Scudder, J. M. 2013, MNRAS, 433, L59
Perez, F., & Granger, B. E. 2007, CSE, 9, 21
Pettitt, A. R., Dobbs, C. L., Acreman, D. M., & Bate, M. R. 2015, MNRAS, 449, 3911
Pettitt, A. R., Tasker, E. J., & Wadsley, J. W. 2016, MNRAS, 458, 3990
Pettitt, A. R., Tasker, E. J., Wadsley, J. W., Keller, B. W., & Benincasa, S. M. 2017, MNRAS, 468, 4189
Pettitt, A. R., & Wadsley, J. W. 2018, MNRAS, 474, 5645
Pontzen, A., Roškar, R., Stinson, G., & Woods, R. 2013, Pynbody: N-Body/SPH analysis for python, Astrophysics Source Code Library, ascl:1305.002
Prandoni, I., Iovino, A., & MacGillivray, H. T. 1994, AJ, 107, 1235
Randriamanakoto, Z. 2015, PhD thesis, Department of Astronomy, Univ. of Cape Town
Randriamanakoto, Z., & Väisänen, P. 2017, in IAU Symp. 316, Formation, Evolution, and Survival of Massive Star Clusters, ed. C. Charbonnel & A. Nota, 70
Randriamanakoto, Z., Väisänen, P., Ryder, S., et al. 2013, MNRAS, 431, 554
Reid, M. J., Schneps, M. H., Moran, J. M., et al. 1988, ApJ, 330, 809
Renaud, F., Bournaud, F., & Duc, P.-A. 2015, MNRAS, 446, 2038
Richter, O.-G., Sackett, P. D., & Sparke, L. S. 1994, AJ, 107, 99
Rieke, G. H., Young, E. T., Cadien, J., et al. 2004, Proc. SPIE, 5487, 50
Robitaille, T., & Bressert, E. 2012, APLpy: Astronomical Plotting Library in Python, Astrophysics Source Code Library, ascl:1208.017
Sabater, J., Best, P. N., & Argudo-Fernández, M. 2013, MNRAS, 430, 638
Saito, T., Iono, D., Espada, D., et al. 2017a, ApJ, 834, 6
Saito, T., Iono, D., Xu, C. K., et al. 2016, PASJ, 68, 20
Saito, T., Iono, D., Xu, C. K., et al. 2017b, ApJ, 835, 174
Saito, T., Iono, D., Yun, M. S., et al. 2015, ApJ, 803, 60
Sakamoto, K., Okumura, S. K., Ishizuki, S., & Scoville, N. Z. 1999, ApJ, 525, 691
Sanders, D. B., Mazzarella, J. M., Kim, D.-C., Surace, J. A., & Soifer, B. T. 2003, AJ, 126, 1607
Sanders, D. B., & Mirabel, I. F. 1996, ARA&A, 34, 749
Sanders, D. B., Scoville, N. Z., & Soifer, B. T. 1991, ApJ, 370, 158
Sault, R. J., Teuben, P. J., & Wright, M. C. H. 1995, in ASP Conf. Ser. 77, Astronomical Data Analysis Software and Systems IV, ed. R. A. Shaw, H. E. Payne, & J. J. E. Hayes (San Francisco, CA: ASP), 433
Schmitt, H. R., Calzetti, D., Armus, L., et al. 2006a, ApJS, 164, 52
Schmitt, H. R., Calzetti, D., Armus, L., et al. 2006b, ApJ, 643, 173
Scudder, J. M., Ellison, S. L., Torrey, P., Patton, D. R., & Mendel, J. T. 2012, MNRAS, 426, 549
Sliwa, K., Wilson, C. D., Matsushita, S., et al. 2017, ApJ, 840, 8
Sliwa, K., Wilson, C. D., Petitpas, G. R., et al. 2012, ApJ, 753, 46
Smith, B. J., Struck, C., Hancock, M., et al. 2007, AJ, 133, 791
Solomon, P. M., & Vanden Bout, P. A. 2005, ARA&A, 43, 677
Springel, V., White, S. D. M., Jenkins, A., et al. 2005, Natur, 435, 629
Struck, C., Dobbs, C. L., & Hwang, J.-S. 2011, MNRAS, 414, 2498
Tateuchi, K., Konishi, M., Motohara, K., et al. 2015, ApJS, 217, 1
Teyssier, R., Chapon, D., & Bournaud, F. 2010, ApJL, 720, L149
The Astropy Collaboration, Price-Whelan, A. M., Sipócz, B. M., et al. 2018, arXiv:1801.02634
Thomas, H. C., Dunne, L., Clemens, M. S., et al. 2002, MNRAS, 329, 747
Toomre, A., & Toomre, J. 1972, ApJ, 178, 623
Turner, J. L., Beck, S. C., Benford, D. J., et al. 2015, Natur, 519, 331
Tutukov, A. V., & Fedorova, A. V. 2006, ARep, 50, 785
U, V., Sanders, D. B., Mazzarella, J. M., et al. 2012, ApJS, 203, 9
Ueda, J., Iono, D., Yun, M. S., et al. 2014, ApJS, 214, 1
Van Der Walt, S., Colbert, S. C., & Varoquaux, G. 2011, arXiv:1102.1523
Veilleux, S., Kim, D.-C., Sanders, D. B., Mazzarella, J. M., & Soifer, B. T. 1995, ApJS, 98, 171
Verdes-Montenegro, L., Sulentic, J., Lisenfeld, U., et al. 2005, A&A, 436, 443
Verley, S., Leon, S., Verdes-Montenegro, L., et al. 2007, A&A, 472, 121
Wada, K., Baba, J., & Saitoh, T. R. 2011, ApJ, 735, 1
Wadsley, J. W., Keller, B. W., & Quinn, T. R. 2017, MNRAS, 471, 2357
Werner, M. W., Roellig, T. L., Low, F. J., et al. 2004, ApJS, 154, 1
Whitmore, B. C., Chandar, R., & Fall, S. M. 2007, AJ, 133, 1067
Whitmore, B. C., & Schweizer, F. 1995, AJ, 109, 960
Wilson, C. D., Petitpas, G. R., Iono, D., et al. 2008, ApJS, 178, 189
Woods, D. F., & Geller, M. J. 2007, AJ, 134, 527
Wu, H., Cao, C., Hao, C.-N., et al. 2005, ApJ, 632, L79
Xu, C. K., Cao, C., Lu, N., et al. 2014, ApJ, 787, 48
Yamashita, T., Komugi, S., Matsuhara, H., et al. 2017, ApJ, 844, 96
Yao, L., Seaquist, E. R., Kuno, N., & Dunne, L. 2003, ApJ, 588, 771
Yun, M. S., & Carilli, C. L. 2002, ApJ, 568, 88
Zink, E. C., Lester, D. F., Doppmann, G., & Harvey, P. M. 2000, ApJS, 131, 413